David Bischof, BSc

Experimental Validation of an Ejector for a stationary Fuel Cell System

Master's Thesis

Electrical Engineering

Graz University of Technology

Institute of Electricity Economics and Energy Innovation

University Supervisors

Assoc.Prof. Dr. Udo Bachhiesl
Dr. Jürgen Fabian

Company Supervisor AVL List GmbH

Dr. Martin Hauth

Graz
October 2017

Acknowledgements

I would first like to thank my university advisor Dr. Jürgen Fabian for his consistent support whenever needed. Moreover, the door to Assoc.Prof. Dr. Udo Bachhiesl and Dr. Martin Hauth's office was always open whenever I ran into a trouble spot or had a question about my research or writing. Thank you for the assistance.

I would also like to thank the experts and friends who were involved in the thesis, laboratory work and personal exchange: Nikolaus Soukup, Christopher Sallai, Michael Seidl, Philipp Maximilian Richter, Stefan Planitzer, Mirko Rossi, Matej Tkaucic, Matthias Bajzek, Marika Natalie Gasteiger, Horst Kiegerl, Jörg Mathe, Juritsch Dominik, Daniel Krems, Dirk Denger, Fabian Obermayer, René Vötter as well as Marcus, René and Christian from the Fuel Cell Laboratory. Without their passionate participation and input, the measurements and validation could not have been so successfully conducted. I'm also very thankful for all the support coming from the Systems-Engineering students (SE-Lab) of AVL.

I would also like to acknowledge DI Nikolaus Soukup as the second reader of this thesis, and I am grateful for his valuable comments.

Finally, I must express my very profound gratitude to my girl Barbara, her brother Stefan with Elisa and to my parents and sisters for providing me with support and encouragement throughout my years of study and through the process of researching and writing this thesis. Thank you!

David Bischof

Statutory Declaration

I declare that I have authored this thesis independently, that I have not used other than the declared sources/resources, and that I have explicitly marked all material which has been quoted either literally or by content from the used sources.

Graz, _____ _____

Date Signature

Abstract

This thesis deals with the performance evaluation of an ejector for a stationary $3-6\,\mathrm{kW}$ electrical output solid oxide fuel cell system (SOFC) with combined heat and power generation (CHP) of AVL List GmbH. Furthermore, the computational fluid dynamic (CFD) simulations of the ejector containing a Laval nozzle are to be validated with experimental data. Therefore, a test rig was designed and constructed in order to simulate the operating conditions for the ejector. The rig also contains instrumentation for analyzing the pressure and general flow distribution inside of the system.

The process products on the anode-side of the fuel cell are reused as they still contain hydrogen, carbon monoxide, steam as well as thermal energy. This process is called anode-off gas recirculation (AGR) and is realized by using a high temperature blower. This component inside of the recirculation path is needed for adapting the recirculation ratio according to the fuel cell process. The steam coming off the anode is being harnessed in the reformation process of the fuel gas. The recirculation leads to a high fuel utilization and consequently to a higher degree of the overall system efficiency.

The idea of the present thesis was to replace the blower in the anode path by an ejector which is a robust and relatively cheap component with less maintenance effort compared to the blower. Additionally, the electrical efficiency of the system could be increased by replacing this component. The results of the work basically showed that it is not possible to reach the required performance parameters for this application with the proposed design of the ejector system. Nevertheless, the CFD simulations for the operation with cold air correlate very well with the information gained from the measurements. This allows working on further design investigations and consequential improvements with respect to the ejector efficiency.

The thesis has been carried out at the Fuel Cell Department (PTE-DRF) of AVL List GmbH in Graz, Austria, in collaboration with the Institute of Electricity Economics and Energy Innovation (IEE) which is a part of Graz University of Technology.

Kurzfassung

Diese Arbeit beschäftigt sich mit der Untersuchung eines Ejektors für ein stationäres Festoxid-Brennstoffzellensystem mit einer elektrischen Ausgangsleistung von $3 - 6\,\mathrm{kW}$ und einer zusätzlichen Wärmeauskopplung der AVL List GmbH. Die vorhandenen Strömungssimulationen des Ejektors inklusive der enthaltenen Laval Düse sollen mit Hilfe von experimentellen Messdaten validiert werden. Um die Randbedingungen der Simulation herstellen zu können, soll ein Prüfstand entwickelt und gefertigt werden. Dieser Aufbau soll unter anderem Rückschlüsse auf das Strömungs- und Druckverhalten innerhalb der Ejektors ermöglichen.

Das Brenngas Methan wird im Anodenpfad reformiert um dem Kohlenstoff vom Wasserstoff zu trennen. In dieser Reaktion wird Wasserdampf und thermische Energie benötigt. Die anodenseitigen Prozessprodukte der Brennstoffzelle beinhalten nach wie vor Teile von Wasserstoff, Kohlenmonoxid, Wasserdampf und thermische Energie, weshalb sie innerhalb des Anodenpfades rezykliert werden. Dies führt zu einer Eröhung der Brennstoff-Ausnutzung sowie des Gesamtwirkungsgrades. Die Bezeichung für dieses Vorgehen lautet *Anoden-Abgas Rezirkulation* (AGR) und wird durch die Verwendung eines Hochtemperatur-Verdichters berwerkstelligt. Diese Komponente wird benötigt, um den Grad der Rezirkulation an den Brennstoffzellen-Prozess anzupassen.

Das erklärte Ziel ist das Ersetzen des vorhandenen Verdichters durch einen Ejektor, welcher eine robuste sowie vergleichsweise günstige Komponente mit einem geringeren Wartungsaufwand darstellt. Die Ergebnisse der Arbeit zeigen auf, dass das primär entwickelte Design von Düse und Ejektor die gestellten Leistungsanforderungen nicht erreichen kann. Die Vergleiche zwischen den Strömungssimulationen und Messdaten zeigen dahingegen eine hohe Übereinstimmung. Dies bildet die Grundlage für weitere Verbesserungen bezüglich der Dimensionierung des Ejektors.

Die Arbeit wurde in der Abteilung für stationäre Hochtemperatur-Brennstoffzellen der AVL List GmbH in Zusammenarbeit mit dem Institut für Elektrizitätswirtschaft und Energieinnovation der TU Graz verfasst.

Symbols and Acronyms

AVL	Anstalt für Verbrennungskraftmaschinen List
M, Ma	Mach number
ER	Entrainment ratio
AGR	Anode-off gas recirculation
$\dot{m}$	Mass flow
$\dot{V}$	Volume flow
T	Temperature
P	Pressure (static)
$P_{ambient}$	Ambient pressure (static)
AC	Alternating Current
DC	Direct Current
BoP	Balance of Plant
CHP	Combined Heat and Power
DG	Distributed Generation
FC	Fuel Cell
H	Enthalpy
LHV	Lower Heating Value
NG	Natural Gas
R	Ideal gas constant
S	Entropy
SOFC	Solide Oxide Fuel Cell
ASC	Anodic supplied cell
ESC	Electrolytic supplied cell
CO	Carbon Monoxide
CO_2	Carbon Dioxide
CH_4	Methane
N	Nitrogen
O_2	Oxygen
C	Carbon
NO_x	Nitrous gases
H_2O	Water (or steam)
γ	Heat capacity ratio
c	Speed of sound
OXCAT	Oxidation Catalyst

Contents

1 Fuel Cells

The availability of electrical energy has been a crucial factor for a sustainable development of modern society. Most of it is still produced from fossil fuels such as oil, coal and natural gas which are non renewable sources and do have a major negative impact on our environment and the earth's climate.

1.1 Why fuel cells?

In the development of future energy conversion systems there is a high attention on technologies which are environmentally friendly and offer a high energy efficiency. The use of innovative fuel cell systems can enable such a transition towards more sustainability and clean energy conversion solutions.

Some advantages of a fuel cell as an energy converter are [1]:

- *Efficiency.* Fuels cells are generally more efficient than piston or turbine based combustion engines. Furthermore this advantage is also true for small size application of fuel cells. This is especially interesting when looking at small local power generating systems with combined heat and power generation.
- *Simplicity.* The basic construction of the fuel cell does contain only a few if any moving parts. Also the conversion of chemically bound energy into electrical energy is happening directly.
- *Low emission.* When using hydrogen as a fuel, the by-product is pure water meaning that the fuel cell reaction itself works with *zero emission*. This is one of the major advantages of the use in vehicles, as there the requirement for emission reduction is becoming more important than ever. Nevertheless, there is mostly an emission of CO_2 involved when it comes to the production of hydrogen.

1.2 What is a fuel cell?

A fuel cell is an electrochemical device which converts chemical energy stored in a fuel directly into electrical energy without passing through the combustion process [2]. The supply of fuel and oxygen (mostly from air) allows a continuous energy conversion process.

Transforming energy stored chemically in a fuel to electricity by means of an internal combustion engine is done in three steps as pointed out in Figure 1.1. Through each conversion step the overall efficiency is being reduced. In this application the fuel cell performs better through the direct transformation, making higher degrees of efficiency possible.

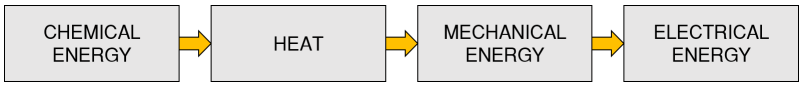

Figure 1.1: Generating electrical energy by means of an internal combustion engine

Figure 1.2 and 1.3 show a basic difference between conventional battery and fuel cell systems with respect to the transformation of energy. The battery is used for application where cyclic conversion is needed. In the case of the fuel cell, the energy flow is unidirectional but continuous.

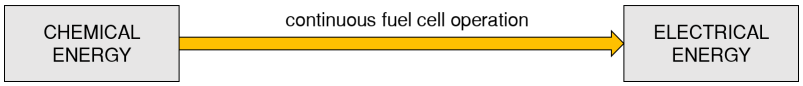

Figure 1.2: Generating electrical energy by means of a fuel cell

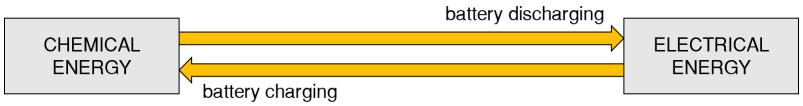

Figure 1.3: Generating electrical energy by means of a battery

1.3 Hydrogen fuel cells - basic principles

The basic working principle of the hydrogen fuel cell is quite easy to understand. The following experiment in Figure 1.4 is used to give a demonstration. When applying direct current to the electrodes, shown in (a), an electric current flows through the water and it will be electrolyzed into hydrogen and oxygen. If the direct current source is being substituted by an ampere meter, the electrolysis is being reversed. A current will flow in the opposite direction and the hydrogen and oxygen are recombining [1].

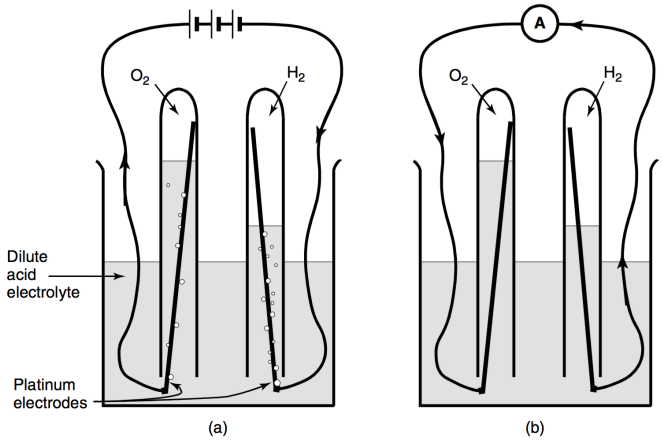

Figure 1.4: Electrode reactions (a) electrolysis and (b) reversed electrolysis / fuel cell reaction [1]

When looking at the chemical reaction that is happening, it can also be said that the fuel is being *burnt* or *combusted*:

$$2H_2 + O_2 \rightarrow 2H_2O \tag{1.1}$$

But instead of liberating a high amount of heat energy like in conventional combustion processes, electrical energy is produced.

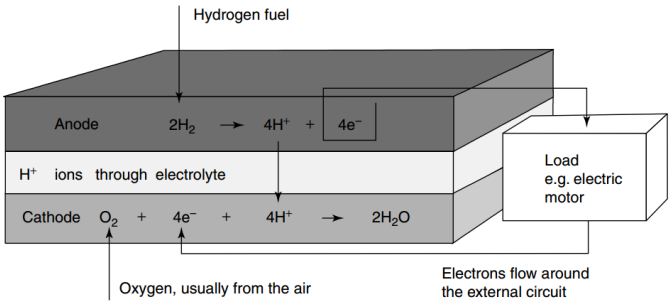

Figure 1.5: Electrode reactions and charge flow for an acid electrolyte fuel cell [1]

At the anode of the acid electrolyte fuel cell, the hydrogen gas ionizes, releasing electrons and creating H^+ ions (or protons).

$$2H_2 \rightarrow 4H^+ + 4e^- \tag{1.2}$$

Energy is released in this reaction. At the cathode, oxygen reacts with electrons taken from the electrode, and H^+ ions from the electrolyte, to form water.

$$O_2 + 4e^- + 4H^+ \rightarrow 2H_2O \tag{1.3}$$

In order to keep this reaction to proceed continuously, the electrons and the H^+ ions which are produced at the anode must travel to the cathode. The ions must

pass through the electrolyte where an acid serves this purpose very well as it is a fluid containing free H^+ ions. But the electrolyte must **only** allow ions to pass through but not the electrons. They are forced to travel over the external electric circuit as shown in Figure 1.5 [1].

1.4 Connecting cells

The voltage produced from one single cell is quite small for energy demanding applications, and is around 0.7 V when a useful current is drawn. Therefore, the cells have to be connected in series to gain a higher output voltage. This results in the known configuration of a stack. In Figure 1.6 the schematic connection is shown neglecting the technical need of feeding oxygen to the cathode and fueling hydrogen to the anode [1].

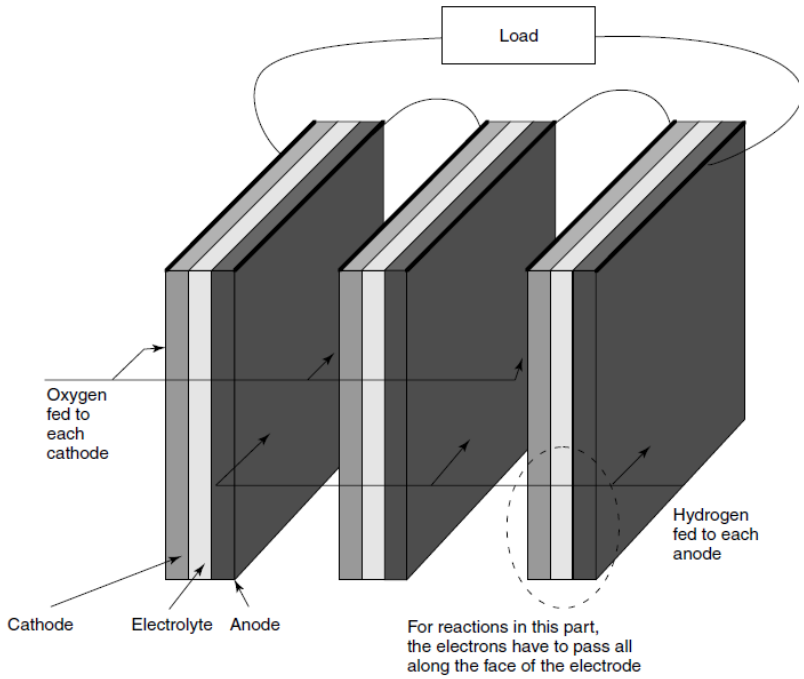

Figure 1.6: Simple edge connection of three cells in series [1]

For tackling the problem of interconnecting the cells a possible solution is shown in Figure 1.7. The bipolar plate with horizontal and vertical grooves on the one and the other side can be used to ensure gas supply on the whole surface of the electrodes. Furthermore, the plates must be a good conductor for the electrical current. The real design of these plates is fairly sophisticated and a great amount of engineering work is related to the enhancement of this part [1].

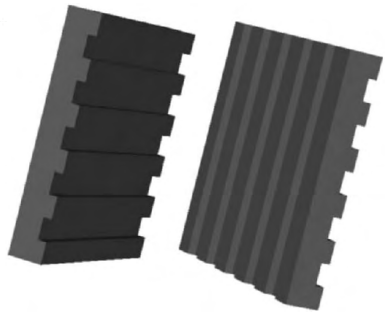

Figure 1.7: Two bipolar plates [1]

Finally, a schematic setup of a three cell stack is depicted in Figure 1.8. The positive and negative electrical connections show, that the current is flowing through all the cells from one to the other side. The bipolar plates which are connecting the cells electrically are also present. Moreover, the porous electrolyte needs to be embedded into a gas-tight gasket on the edges to prevent the gas from streaming out on the edges. The gas leaks are often a major topic in building fuel cell stacks [1].

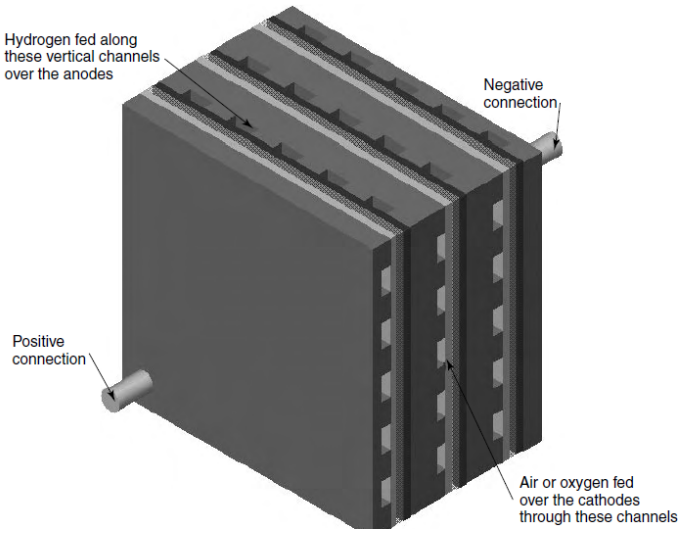

Figure 1.8: A three cell stack showing how bipolar plates connect the anode of one cell to the cathode of its neighbouring cell [1]

1.5 Production of hydrogen from fossil fuels

The share of hydrogen produced from fossil fuels was 96 % in the year 2010. The most common procedure is steam reforming. The reformation of natural gas is done in two steps. Firstly, out of methane and water at high pressure (15 – 25 bar) and high temperature (700 – 1000 °C) carbon monoxide and hydrogen is produced. The reaction is accelerated by using a catalyst. Secondly, by adding water the carbon monoxide is converted to carbon dioxide and hydrogen. The second step is also known as shift–reaction [3].

1.6 Main fuel cell technologies and classification

Fuel cells can mainly be classified after their operating temperature and the used electrolyte. Figure 1.9 shows a comparison of the main fuel cell technologies.

U.S. DEPARTMENT OF ENERGY | Energy Efficiency & Renewable Energy

FUEL CELL TECHNOLOGIES PROGRAM

Comparison of Fuel Cell Technologies

Fuel Cell Type	Common Electrolyte	Operating Temperature	Typical Stack Size	Efficiency	Applications	Advantages	Disadvantages
Polymer Electrolyte Membrane (PEM)	Perfluoro sulfonic acid	50-100°C 122-212° typically 80°C	< 1kW–100kW	60% transportation 35% stationary	• Backup power • Portable power • Distributed generation • Transporation • Specialty vehicles	• Solid electrolyte reduces corrosion & electrolyte management problems • Low temperature • Quick start-up	• Expensive catalysts • Sensitive to fuel impurities • Low temperature waste heat
Alkaline (AFC)	Aqueous solution of potassium hydroxide soaked in a matrix	90-100°C 194-212°F	10–100 kW	60%	• Military • Space	• Cathode reaction faster in alkaline electrolyte, leads to high performance • Low cost components	• Sensitive to CO_2 in fuel and air • Electrolyte management
Phosphoric Acid (PAFC)	Phosphoric acid soaked in a matrix	150-200°C 302-392°F	400 kW 100 kW module	40%	• Distributed generation	• Higher temperature enables CHP • Increased tolerance to fuel impurities	• Pt catalyst • Long start up time • Low current and power
Molten Carbonate (MCFC)	Solution of lithium, sodium, and/or potassium carbonates, soaked in a matrix	600-700°C 1112-1292°F	300 kW-3 MW 300 kW module	45-50%	• Electric utility • Distributed generation	• High efficiency • Fuel flexibility • Can use a variety of catalysts • Suitable for CHP	• High temperature corrosion and breakdown of cell components • Long start up time • Low power density
Solid Oxide (SOFC)	Yttria stabilized zirconia	700-1000°C 1202-1832°F	1 kW–2 MW	60%	• Auxiliary power • Electric utility • Distributed generation	• High efficiency • Fuel flexibility • Can use a variety of catalysts • Solid electrolyte • Suitable for CHP & CHHP • Hybrid/GT cycle	• High temperature corrosion and breakdown of cell components • High temperature operation requires long start up time and limits

For More Information

More information on the Fuel Cell Technologies Program is available at *http://www.hydrogenandfuelcells.energy.gov*.

U.S. DEPARTMENT OF ENERGY
Energy Efficiency & Renewable Energy

EERE Information Center
1-877-EERE-INFO (1-877-337-3463)
www.eere.energy.gov/informationcenter

February 2011

Printed with a renewable-source ink on paper containing at least 50% wastepaper, including 10% post consumer waste.

Figure 1.9: Fuel cell technologies comparison table [4]

1.6.1 PEMFC (Proton Exchange Membrane Fuel Cell)

A distinctive feature of PEM fuel cells is their ability of operating at cooler temperatures (26 to 93 °C) compared to other types. For the electrolyte a polymer membrane is used and for the catalyst a precious metal, typically platinum. Due to the relatively low operating temperatures and the use of precious metals, pure hydrogen is a typical fuel of the PEMFC. The efficiency of operation is between 35 % to 60 % and they can handle sudden and large shifts in power output. PEM fuel cells are therefore qualified for the use in cars and other mobile applications (e.g. forklift) where quick start up and acceleration is demanded [5].

1.6.2 AFC (Alkaline Fuel Cell)

AFCs have been used to provide both electricity and water to the crew of the NASA Apollo mission. They are using an alkaline membrane and a porous electrolyte saturated with an alkaline solution. Using AFCs in combined heat and power (CHP) applications can yield an electrical efficiency of 80 % to 90 %. The cell is very sensitive to carbon dioxide and it can fail when it is exposed to this gas. Therefore, AFCs are used in underwater and controlled aerospace applications primarily [5].

1.6.3 DMFC (Direct Methanol Fuel Cell)

The DMFCs are using a polymer membrane as an electrolyte and commonly also a platinum catalyst much like the PEMFCs. The DMFCs obtain hydrogen from liquid methanol and not directly from hydrogen fuel as the PEMFCs. The operating temperature is also relatively low, between 50 and 120 °C. Their field of application ranges from small electronics, such as laptops and battery chargers, to applications like stationary power supply systems [5].

1.6.4 PAFC (Phosphoric Acid Fuel Cell)

This fuel cell type is comparable to the PEMFC in terms of the operation method and a similar level of efficiency. It uses a ceramic electrolyte with a platinum catalyst and a liquid phosphoric acid. The PAFCs though can handle small amounts of fuel impurities as they run at higher temperature. Typically they are used to not only produce electricity, but also heat for assisting cooling or heating processes. PAFCs can be found in applications demanding a high amount of energy such as schools, hospitals and manufacturing centers [5].

1.6.5 MCFC (Molten Carbonate Fuel Cell)

As an electrolyte, the MCFCs use a molten carbonate-salt mixture suspended in a ceramic matrix. The operating temperature is upwards of 600 °C allowing them to make us of non-platinum catalyst through a process that is called „internal reforming“. The MFCFs can facilitate natural gas as a direct source of fuel, because the high temperatures allow internal reforming of the gas into hydrogen inside of the system. This type of fuel cells are often found in stationary applications where they provide high-quality primary and back-up power to businesses and utilities [5].

1.6.6 SOFC (Solid Oxide Fuel Cell)

Solide oxide fuel cells are operating in the highest temperature range of 315 to 540 °C. For the electrolyte they use a dense layer of ceramics which allows conductivity of oxygen ions at high temperatures. The SOFC can be fueled by natural gas as the non-platinum catalyst enables internal reformation. This allows the SOFC to reach electrical efficiencies of 50 % to 60 %, and 70 to 80 % in CHP applications. Common application of SOFCs are small residential auxiliary power units to supply heat and power to homes. They are also implemented in large stationary power generation systems for large buildings [5].

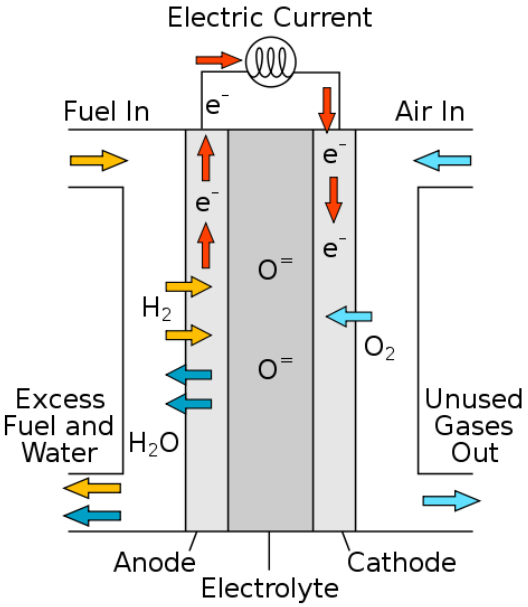

Figure 1.10: Principal working scheme of an SOFC [6]

2 Stationary fuel cell systems

This chapter deals with basic aspects of stationary fuel cell systems in general and the analyzed SOFC system developed at AVL. The high temperature systems use processed fuel and make use of the exhaust heat. This is why they are mainly found in stationary power generation systems. Whereas the the complexity of fuel processing very often rules out the application of high-temperature fuel cells for mobile use [1].

2.1 Stationary CHP fuel cell systems

Figure 2.1 gives a spatial overview of a fuel cell system with combined heat and power generation for a electrical power output of up to 100 kW.

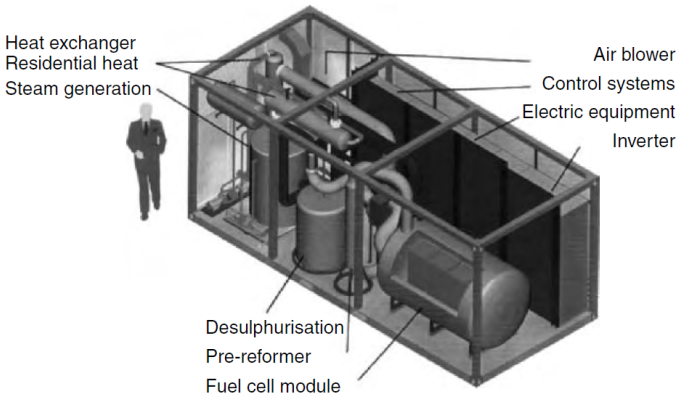

Figure 2.1: Design of a 100 kW fuel cell based combined heat an power system [1]

Figure 2.2 illustrates a functional diagram of a stationary fuel cell system containing the main features. Such a setup could be used in residential areas for generating electricity and hot water out of different types of fuel.

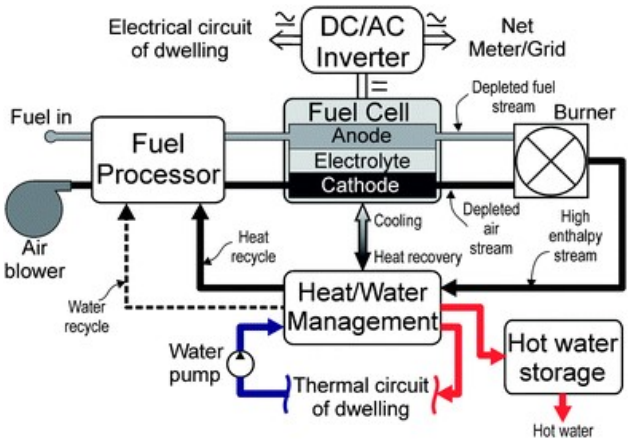

Figure 2.2: Main features of a fuel cell micro-CHP system [7]

Figure 2.3 shows how the system depicted in Figure 2.2 is situated and connected inside of a domestic house. Assuming a fuel cell running at a constant operating point for maximizing the degree of efficiency, electrical energy can be fed back into the electrical power grid when the current electric power demand of the household is lower than the provided electrical power of the fuel cell.

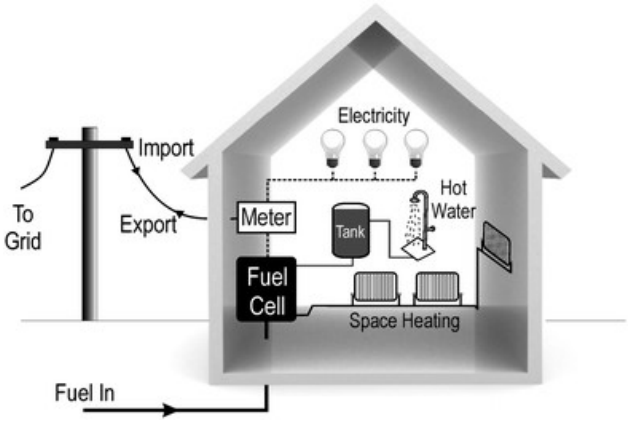

Figure 2.3: The fuel cell micro-CHP concept showing import/export of electricity [7]

The Sankey diagrams in Figure 2.4 compare the supply of electricity and heat for domestic use in two scenarios. The scenario *Power plant & grid with Boiler* on the left assumes, that the electricity is produced from fossil fuel (centralized production) and transported over an electrical grid to the household. The demanded heat is being supplied from a fossil fueled Boiler. In this scenario 180 units of energy are needed. The scenario *Combined Heat and Power* on the right assumes, that the energy is being produced in a decentralized application. The waste heat is being harnessed which will increase the efficiency of this system. Moreover, the losses through transportation of energy are lower. This is a common field of application for stationary fuel cell systems.

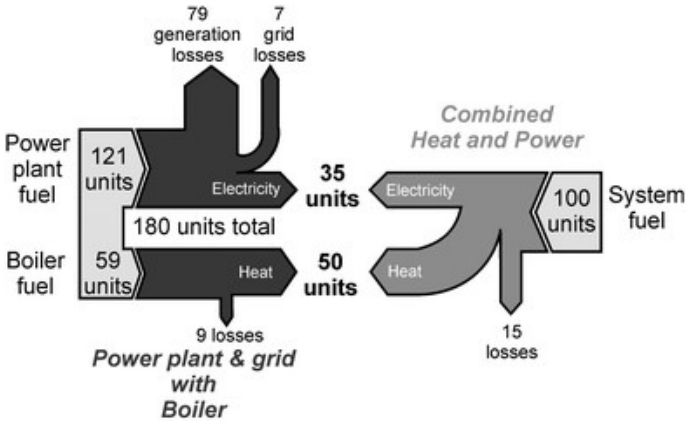

Figure 2.4: Sankey diagrams for household energy supply in two scenarios [7]

2.2 AVL stationary SOFC CHP system

In order to understand how and why an ejector is used inside of a stationary fuel cell system, a basic overview will be given in this chapter. Figure 2.5 shows an image of the current system which is divided into two major modules, the SOFC stack and the gas processing module. The respective design target data are stated in Table 2.1.

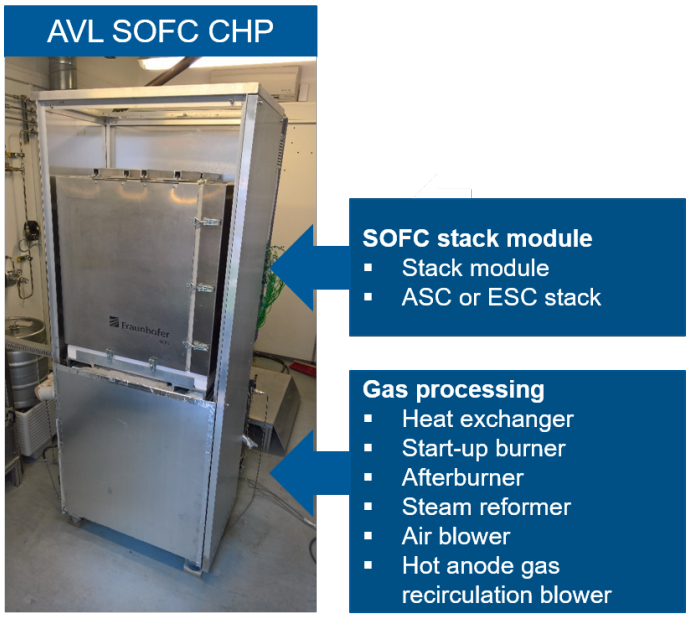

Figure 2.5: AVL SOFC CHP system [8]

Table 2.1: AVL SOFC CHP design target data [9]

Electrical DC power ouput	$3 - 6\,\mathrm{kW}$
Fuel	Natural Gas (NG)
Electrical Efficiency (AC)	$> 55\,\%$
Total Efficiency (CHP)	$> 90\,\%$
Hot gas anode recirculation (AGR)	$< 620\,^{\circ}\mathrm{C}$
Production cost target	$< 2000\,€/\mathrm{kW}$
CO Emissions	$< 50\,\mathrm{mg/kWh}$
NO_x Emissions	$< 40\,\mathrm{mg/kWh}$

In the following paragraph an explanation of the AVL SOFC system for stationary applications will be given. The respective flowchart for steady-state conditions is presented in Figure 2.6. In the real system an auxiliary start-up unit is used. The red path shows the anode line and the blue path refers to the cathode line. The exhaust line is coloured orange. The different components of the system are marked with the numbers from 1 to 10 and named as follows:

1. anode line inlet
2. anode line blower
3. pre – reformer
4. anode line heat exchanger
5. stack module
6. cathode line inlet
7. cathode line blower
8. cathode line heat exchanger
9. afterburner (oxidation catalyst / OXICAT)
10. exhaust gas heat exchanger

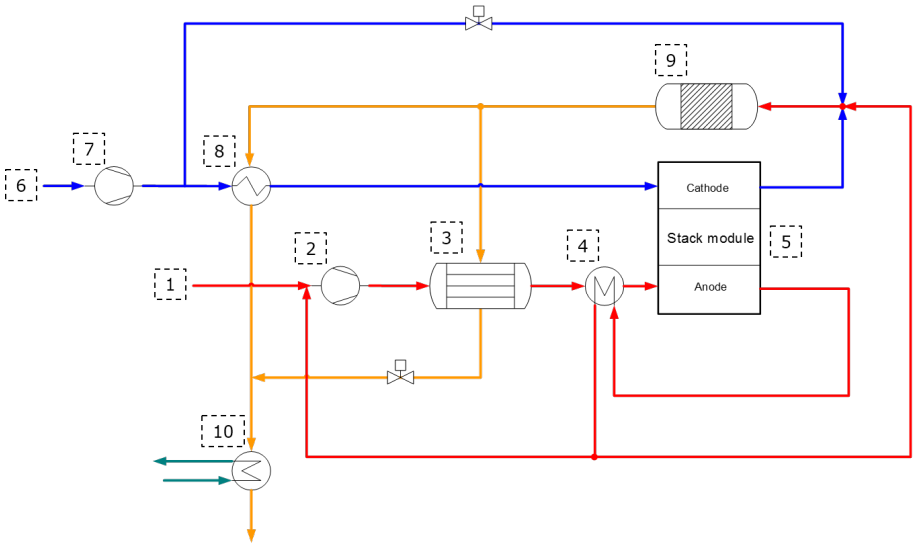

Figure 2.6: SOFC system – process flow diagram [8]

At the anode line inlet the natural gas is fed to the system. Afterwards, there is a junction where the anode-off gas is being added. This process is being described as anode-off gas recirculation (AGR) and is useful to supply steam and hot gases for the pre-reformer in order to increase the efficiency of the system.

The pre-reformer is then used to reform the natural gas in order to achieve a mixture of gas containing a high amount of hydrogen H_2. Other side products of the reformation gas are carbon monoxide CO, carbon dioxide CO_2 as well as steam H_2O and methane CH_4. This is done because a too high methane content at the stack module anode inlet can lead to extensive cooling of the stacks due to the resulting endothermic internal reformation reaction. For a proper functioning of the pre-reformer it is critical to have enough steam to avoid carbon deposition issues inside the catalyst.

To heat up the gas mixture entering the anode side of the stack module, the anode line heat exchanger is being used. A catalytic combustion of the exhaust gases containing hydrogen and carbon monoxide is performed in the afterburner, also known as oxidation catalyst. To keep the combustion temperatures in the afterburner under control, an extra fresh air line is provided. Furthermore, the heat generated from the afterburner is applied to warm up the fresh air coming from the cathode line inlet and also the pre-reformer.

In the stack module the electrochemical reactions take place producing heat and electrical power in the form of direct current (DC). The electrical connectors are not shown in this process flow diagram. The remaining heat of the exhaust gases can be used for cogenerative purposes by means of the exhaust gas heat exchanger.

However, for the proper functioning of the system, extra instrumentation such as pressure and temperature sensors, mass flow controllers, control throttles and a start-up system as well as a system control unit are needed. To make use of the electrical energy in alternating current (AC) environments also a power processing unit called inverter must be installed.

The power consumption of the anode gas recirculation blower in Figure 2.7 is significant for the electrical efficiency of the system. The blower operates at an isentropic efficiency of 60 % [10].

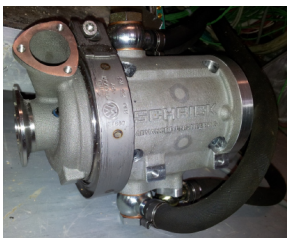

Figure 2.7: Anode gas recirculation blower (AVL Schrick) [11]

3 Development Process

The overall process of developing and validating an ejector system for a stationary fuel cell system is depicted in Figure 3.1. The target is to increase the electrical efficiency of the current AVL SOFC system by using an ejector inside of the anode path instead of a high temperature blower.

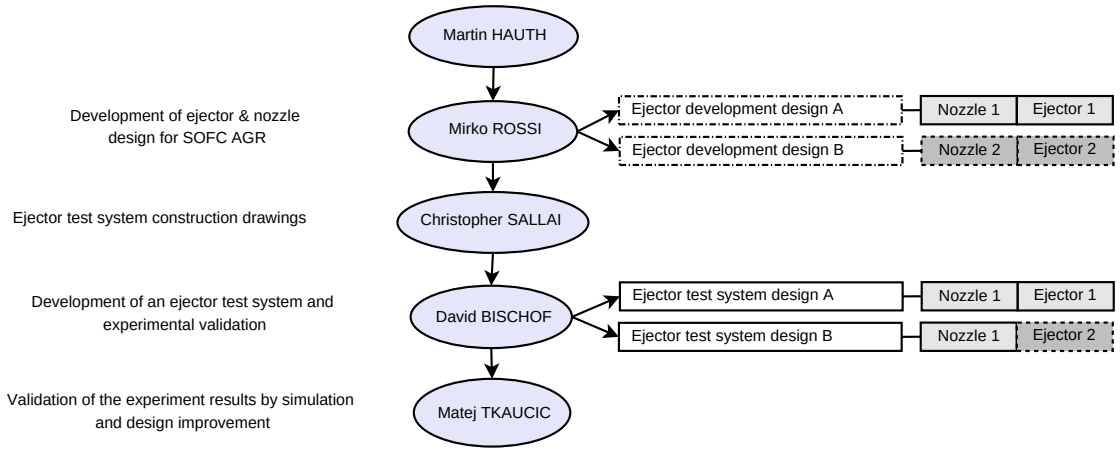

Figure 3.1: SOFC ejector system development process

Dr. Martin Hauth is the Lead Engineer of the stationary SOFC fuel cell systems at AVL in Graz (Austria). The major development part on the ejector system and the nozzle design was done by M. Rossi and is described in his master thesis [12]. Based on his simulations performed with AVL Fire including his calculations and design suggestions found from literature, he developed two basic designs as shown in Figure 3.1. Most of his assumptions are also stated in the dissertation of Liao [13]. The ejector of M. Rossi was designed for the use of cold air as a primary inlet gas.

In the second step, in close contact with C. Sallai (AVL), a test system setup containing the ejector was developed and subsequently constructed using PTC Creo. The aim was to validate the CFD simulations in order to proceed in making an improved ejector design for the operation with methane as a primary gas and temperatures in the suction chamber of up to 600 °C. Therefore, different system pressure losses must be reproducible to reveal results that are comparable to the analyzed operating conditions of the fuel cell system. This was done by using two metal flanges in the representative anode path and also in the anode recirculation path of the test rig. By means of the flanges metal orifices with different

diameters can the be brought into the system and still guarantee gas tightness. For determining the conditions inside of the ejector, pressure and temperature sensors were used. Furthermore, a measurement of the volume flow inside of the system was realized with a Venturi pipe. The value for the volume flow that is brought into the system through the primary inlet of the ejector is taken from the actual value of the mass flow controller.

Following, the experimental validation was performed in the fuel cell laboratory of AVL. The results were then discussed with the SOFC fuel cell team in order to get a better understanding of the working principle of the ejector. All measurement results and performance influencing parameters are stated in this work.

The results of the experiments on **Ejector test system design A** and **B** are furthermore to analyze by M. Tkaucic. The design investigations, based on the actual test system, are described in his master thesis [14]. The simulations done by M. Rossi are based on a simplified ejector design.

The main parameters of M. Rossis development designs are shown in Table 3.1 [12]. He changed all of the major parameters regarding the nozzle and the ejector system as a whole.

Table 3.1: Main parameters of the Ejector development designs [12]

		Ejector development design	
		A	**B**
Nozzle throat diameter	d_T	0.80 mm	0.58 mm
Nozzle exit diameter	d_{NE}	0.87 mm	0.91 mm
Ejector mixing chamber diameter	d_c	10.50 mm	6.00 mm
Ejector mixing chamber length	l_c	70.40 mm	67.09 mm

4 Ejector

This chapter deals with ejectors in general, showing the major components, working principle and operation modes. Moreover, applications of ejectors are described. Also information on nozzles, which are a fundamental element, is provided in this chapter. Then the use of ejectors in stationary fuel cell systems is described briefly and afterwards the simulation results of the first developed ejector design are presented.

4.1 What is an ejector?

An ejector is a common fluid machine where a propelling stream can be used to suck in fluids or gases and mix them. The basic construction elements shown in Figure 4.1 are the following:

1. secondary inlet (suction)
2. primary nozzle
3. primary inlet (motive or propellant)
4. suction chamber
5. mixing chamber and diffusor

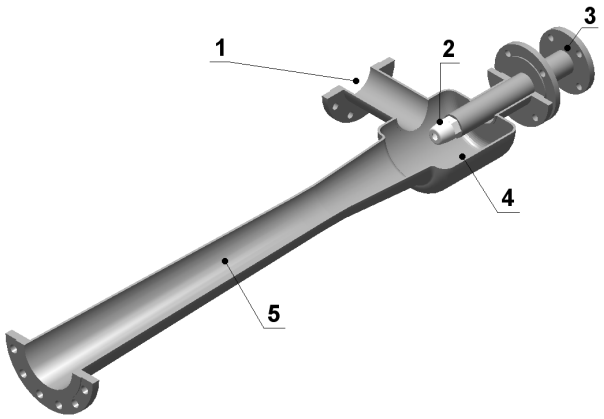

Figure 4.1: Sectional view of a steam ejector [15]

The main advantages of using an ejector instead of a rotational pump (blower or compressor) are:

- The ejector is very robust because there are no moving parts.
- It can operate at high temperatures.
- The maintenance costs are low compared to a blower.
- No electricity needed.

Figure 4.2 shows an ejector with a straight mixing chamber and the mainly used indexes which are explained in Table 4.2.

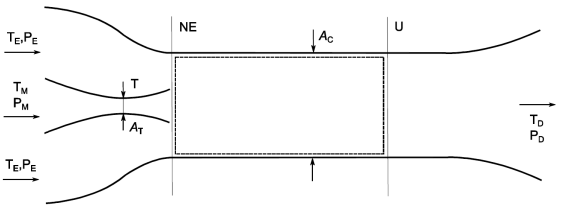

Figure 4.2: Schematic diagram of a straight mixing chamber ejector [16]

Table 4.1: Explanation of indexes used in Figure 4.2 [16]

C	mixing chamber area
D	discharge
E	entrained gas or fluid
M	motive gas or fluid
NE	motive nozzle exit
T	motive nozzle throat
U	uniform flow cross section

The following rules can be applied regarding the use of the term ejector or injector:

- The term **ejector** is used for pumps which create a local vacuum. The device has mainly the purpose of sucking a secondary medium.
- The term **injector** is generally used for pumps that create a local overpressure. These devices have mainly the purpose of compressing a medium.

Unfortunately the use of the different terms is inconsistent. Therefore, both of the terms can be found in literature for the different fields of application.

4.2 Gas ejector working principle

First of all, the primary gas is pressurized. This is the main source of energy the ejector makes use of. The difference in pressure over the nozzle accelerates the gas in the direction of the nozzle exit and consequently to the suction chamber area. The expansion of the motive gas at the nozzle exit results in a local low pressure

region. This will cause the gas in the secondary path to be sucked towards the mixing chamber area. The entrainment of the secondary gas will slow down the high velocity motive stream in the mixing chamber and a new velocity pattern is shaped. Moreover, the two gases are mixed inside of this region. The diffuser at the end of the ejector is needed to regain pressure from the kinetic energy of the fast moving stream inside of the mixing chamber [1].

4.2.1 Ejector parameter

The entrainment ratio (ER) is defined as the ratio between the secondary mass flow $\dot{m}_s$ and the primary mass flow $\dot{m}_p$ [13]:

$$ER = \frac{\dot{m}_s}{\dot{m}_p} \tag{4.1}$$

When using the same gas in the primary and secondary inlet in the ejector test, the entrainment ratio can be calculated from the respective volume flow at standard conditions[1]. This is because the densities of the primary and secondary gas are the same. The mass flow can be calculated by multiplying the density and the volume flow at standard conditions:

$$\dot{m} = \rho_N \dot{V}_N \tag{4.2}$$

As a result in this special case the entrainment ratio can be calculated as follows:

$$ER = \frac{\dot{m}_s}{\dot{m}_p} = \frac{\rho_{air}\dot{V}_s}{\rho_{air}\dot{V}_p} = \frac{\dot{V}_s}{\dot{V}_p} \tag{4.3}$$

4.2.2 Ejector operating modes

As shown in Figure 4.3 and Figure 4.4 the operational modes of the ejector can be split into three sections depending on the primary pressure [18]. It can be stated that the primary mass flow is increasing with the primary inlet pressure.

Back flow (0 - P_{Pe})
No mass flow towards the favored flow direction as the pressure inside of the mixing chamber is higher than in the suction inlet. Increasing the pressure slightly over P_{Pe} the ejector starts entraining (denoted by using the index character **e**).

Subcritical mode (P_{Pe} - P_{Pc})
The secondary flow increases strongly with the primary inlet pressure. The flow velocity inside of the nozzle is subsonic and incompressible (Mach number $M < 0.3$). In the converging section the velocity is increased and in the diverging section decreased. The highest value of the entrainment ratio is reached at the

[1]Standard conditions: ($p_N = 1013.25\,\text{bar}$, $T_N = 273.15\,\text{K}$ and $\rho_{N,air} = 1.29\ \text{kg/m}^3$) [17]

transition point to the critical mode where the primary pressure equals the critical pressure P_{Pc} (denoted by using the index character **c**).

Critical mode ($P > P_{Pc}$)
Critical conditions in the nozzle throat are defined as the state where Mach number is unity [13]. Initially the secondary flow is decreasing in the critical mode until it reaches a region where it stays relatively constant. The critical mode is also referred to the design operation mode where the ejector is meant to be operated in.

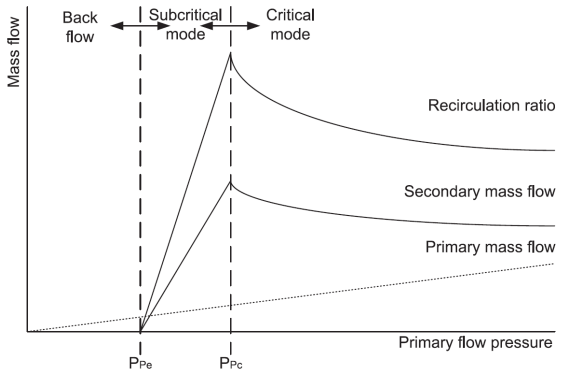

Figure 4.3: Ejector characteristics in different modes, mass flow over primary flow pressure [19]

Figure 4.4 shows the operation modes for three different primary pressures with respect to the back pressure of the ejector. The sequence of the modes is opposite with respect to Figure 4.3. Looking at the graph for P_1 the entrainment ratio is independent of the back pressure until reaching the critical value indicated with a vertical line. Increasing the back pressure over this point, the entrainment ratio is decreased rapidly when finally the back flow mode is reached where no flow towards ejector exit occurs.

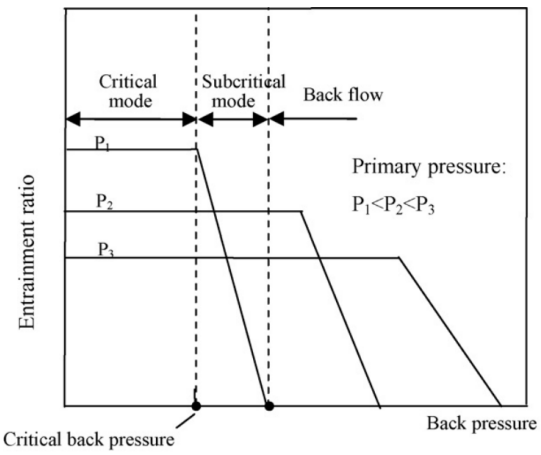

Figure 4.4: Ejector characteristics in different modes, entrainment ratio over back pressure [18]

4.3 Where are ejectors being used?

For the primary medium as well as the secondary medium principally all different kinds of fluids (e.g. liquid, gas, steam, fluid suspension, aerosol) can be used. Therefore, a lot of different fields of application for ejectors are possible. In the following some examples of application regarding the aggregate phase of the primary and secondary medium are shown.

The Aspirator shown in Figure 4.5 is a pumping device used in chemistry and biology laboratories. The low-strength vacuum produced by the working fluid is often used for solvent removal [20].

Figure 4.5: primary=liquid, suction=gas or liquid: Aspirator (pump) [21]

The Bunsen burner shown in Figure 4.6 is named after the german chemist Robert Bunsen and is a common laboratory device for providing a very hot and clean flame. The hose barb on the left is connected to a gas supply and the needle valve on the right is for adjusting the amount of gas being burnt. Inside of the tube going upwards slots are placed in order to admit air to stream inside and mix with the fuel gas [22].

Figure 4.6: primary=gas (methane), suction=gas (air): Bunsen burner [23]

The airbrush shown in Figure 4.7 is a tool operated with pressurized air in order to spray paint, ink or dye. The same effect is used by the nozzles which are used for spraying perfumes and other liquid media [24].

Figure 4.7: primary=gas (air), suction= liquid (paint): Airbrush [25]

The overall process of sandblasting is also known as *abrasive blasting*. An example is shown in Figure 4.8. A stream of abrasive material is propelled against a surface by using compressed air. This can be done in order to smooth, rough or shape a surface or to remove unwanted areas [26].

Figure 4.8: primary=gas (air), suction=solid (sand): Sandblasting [27]

4.4 Nozzle design for supersonic ejectors

In order to achieve high impulse energy of the pressurized primary gas, a Laval nozzle was chosen. The term goes back to a swedish engineer called Carl Gustav de Laval. The Laval nozzle that is being operated correctly can be described by the following characteristics [28]:

1. converging-diverging shape
2. at the lowest cross-section (throat) sonic speed ($M = 1$) is reached
3. the mass flow through the nozzle is fixed (concept of the *critical* nozzle)
4. in the diverging part after the throat a shockfree supersonic stream is achieved

Figure 4.9 shows the convergent-divergent shape of a Laval nozzle including the respective areas of the Mach number and an arrow indicating the flow direction.

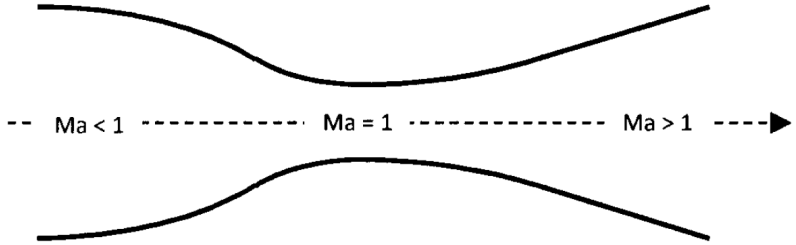

Figure 4.9: Convergent-divergent shape of a Laval nozzle [29]

In fluid dynamics, the Mach number (M or Ma) is a dimensionless quantity representing the ratio of flow velocity past a boundary to the local speed of sound [30].

$$M = \frac{u}{c} \tag{4.4}$$

where:
M is the Mach number
u is the local flow velocity with respect to the boundaries and
c is the speed of sound in the medium

The following derivation describes why a supersonic flow accelerates in the divergent section of a nozzle while the subsonic flow is decelerated in this section. The equations (4.5) to (4.11) are based on *Nozzle Design Converging-Diverging (CD) Nozzle* [31].

Conservation of mass:

$$\dot{m} = \rho V A = constant \tag{4.5}$$

$$\frac{\mathrm{d}\rho}{\rho} + \frac{\mathrm{d}V}{V} + \frac{\mathrm{d}A}{A} = 0 \tag{4.6}$$

Conservation of momentum:

$$\rho V \mathrm{d}V = -\mathrm{d}p \tag{4.7}$$

Isentropic flow:

$$\frac{\mathrm{d}p}{p} = \gamma \frac{\mathrm{d}\rho}{\rho} \tag{4.8}$$

$$\mathrm{d}p = c^2 \mathrm{d}\rho \tag{4.9}$$

Combine with momentum:

$$-M^2 \frac{\mathrm{d}V}{V} = \frac{\mathrm{d}\rho}{\rho} \tag{4.10}$$

Combine with mass:

$$(1 - M^2)\frac{\mathrm{d}V}{V} = -\frac{\mathrm{d}A}{A} \tag{4.11}$$

For subsonic flow ($M < 1$) an increase in area ($\mathrm{d}A > 0$) causes flow velocity to decrease ($\mathrm{d}V < 0$). For supersonic flow ($M > 1$) an increase in area ($\mathrm{d}A > 0$) causes flow velocity to increase ($\mathrm{d}V > 0$). This results in the need for a converging-diverging shape of the nozzle to realize supersonic outflow assuming a subsonic inflow.

4.5 Ejector in a fuel cell system

Figure 4.10 shows the position of the ejector inside of an SOFC system with respect to the system explained in Section 2.2. The ejector is situated at the junction between the primary inlet connection and the anode recirculation path.

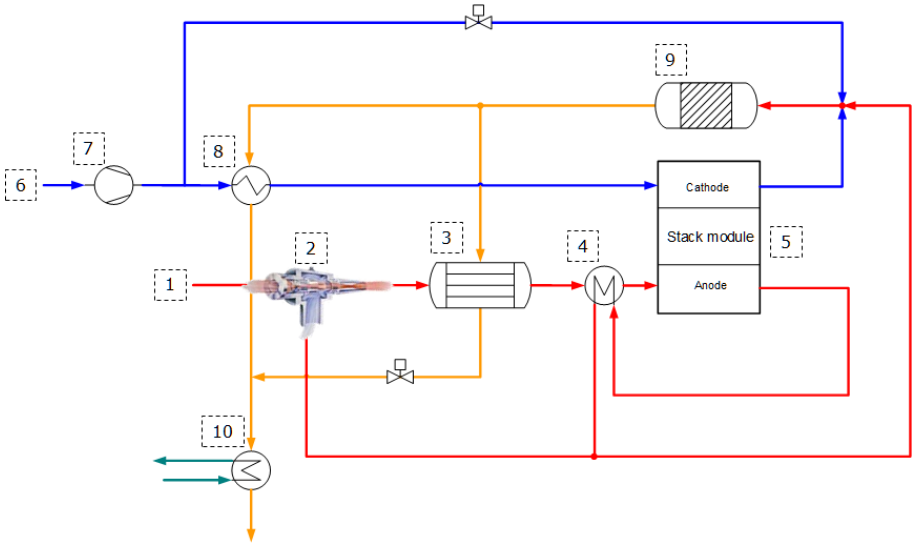

Figure 4.10: AVL SOFC System process flow diagram

The anode off-gas recirculation ratio (AGR) is defined as the ratio of the mass flow being recirculated to the mass flow coming from the anode of the fuel cell stack outlet depicted in Figure 4.11:

$$AGR = \frac{\dot{m}_{\text{recirculate}}}{\dot{m}_{\text{anode-off}}} \tag{4.12}$$

In a complete SOFC system simulation performed at the fuel cell department it was found that the system works well at a recirculation ratio of 70 %. This ratio is defined by the steam to carbon ratio inside of the reformer to prevent carbon deposition.

Figure 4.11 show the flow chart of the extracted sub system used for the design of the ejector. Also the names of the respective flows inside of the SOFC system in Figure 4.10 are stated.

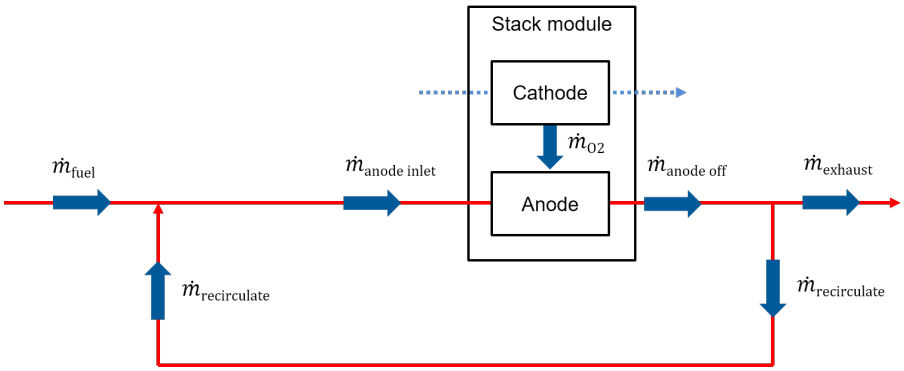

Figure 4.11: SOFC system (anode-path)

4.6 Ejector in the test rig

The ejector test rig is an abstraction of the anode path. Therefore, it is important to understand that in the real SOFC system through the chemical reaction inside of the stack, a certain amount of oxygen $\dot{m}_{O_2}$ travels from the cathode to the anode side of the stack and is therefore included in the flow $\dot{m}_{\text{anode off}}$ coming from the stack. In the ejector test rig there is no input line for oxygen because this would only lead to an increase in friction along the anode-off and exhaust line because of the higher mass flow but otherwise have no influence on the entrainment ratio of the ejector. This friction was simulated by using the *Orifice Stack* shown in Figure 4.12 and described more in detail in Figure 5.1.

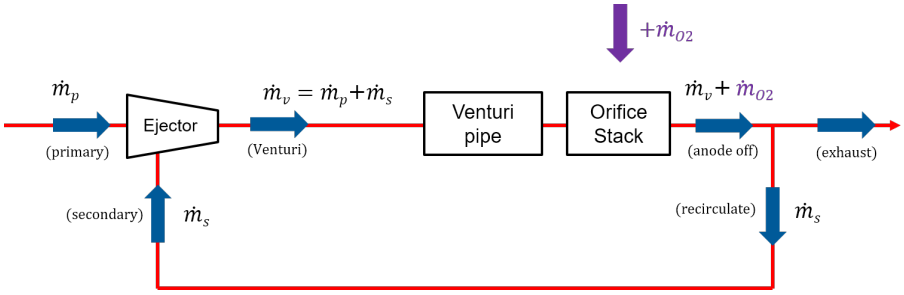

Figure 4.12: Ejector test system setup (simulation of SOFC anode-path)

To ensure that the calculated value of the AGR is comparable to the full system simulations, a fictive variable is introduced:

$$AGR_{O2} = \frac{\dot{m}_{\text{recirculate}}}{\dot{m}_{\text{anode inlet}} + \dot{m}_{O_2}} \tag{4.13}$$

4.7 Ejector CFD simulation results

In this chapter the results of the CFD simulations referred to **Ejector development design A** performed by M. Rossi are presented. The overview of the designs is shown in Figure 3.1. The main design parameters can be found in Figure 4.13:

Nozzle 1: Nozzle throat diameter $d_T = 0.8\,\text{mm}$
Nozzle 1: Nozzle exit diameter $d_{NE} = 0.87\,\text{mm}$
Ejector 1: Mixing chamber diameter $d_c = 10.5\,\text{mm}$
Ejector 1: Mixing chamber length $l_c = 70.4\,\text{mm}$
Position: x_0

Figure 4.13: Main design parameters of **Ejector development design A** [12]

Figure 4.14 shows the graphical representation of the ejector system including the three ports (surfaces) that was used for his CFD analysis. Compared to the test rig setup from the laboratory the outlet is not connected to the secondary inlet. It is assumed that this circumstance does have a negligible impact on the simulation results with respect to the measurements in the laboratory.

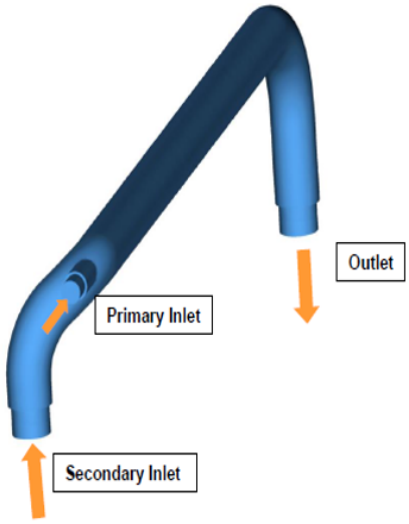

Figure 4.14: Graphical simulation model for CFD analysis on **Ejector development design A** [12]

The data shown in Table 4.2 compromise the main results of M. Rossi's investigations regarding the pressure and flow distribution. The main boundary conditions (BC) are the mass flow rates at the primary $\dot{m}_p$ and the secondary inlet $\dot{m}_s$ surfaces. The target value of $\dot{m}_p = 0.16\,\text{g/s}$ could not be simulated because of errors during the calculation routine of the CFD program. Moreover, he encountered backflow (a flow towards the secondary inlet) when trying to reach the target value. Therefore, he increased the primary inlet mass flow to $0.4\,\text{g/s}$ where the results became stable. In the secondary inlet the mass flow is varied in order to reach a specific entrainment ratio (ER). The pressure on the outlet of the ejector

P_{out} is assumed to be equal to ambient pressure in the simulations. The initial conditions (IC) for all pressures and temperatures on all of the three ports are set according to the values presented. The results of the simulations (R) are the static pressures on the primary inlet P_p and the secondary inlet P_s surfaces as well as the mass flow at the outlet $\dot{m}_{out}$ surface. The pressure at the outlet boundary conditions was set to the reference ambient pressure of 1 bar. The difference in static pressure over the ejector $\Delta P_{ejector}$ is calculated from the simulation results:

$$\Delta P_{ejector} = P_{out} - P_s \tag{4.14}$$

One main result of this simulation was that the pressure difference over the ejector must decrease in order to allow a higher entrainment ratio with a fixed primary inlet mass flow. The target value of $ER = 11$ could not be reached as in Case 6 with $ER = 9$ the pressure difference was already 0 mbar. There are no reasons for this phenomena explained in the thesis of M. Rossi. The link between the CFD simulation and the Matlab-Simulink model is also not mentioned. Moreover, the primary inlet mass flow is twice the design value of the nozzle. Furthermore, no reasons are stated for using $220\,\mathrm{K} = -53,15\,^{\circ}\mathrm{C}$ as an initial temperature.

Table 4.2: CFD simulation results (**Ejector development design A**) [12]

		BC	BC	BC	IC	IC	R	R	R	R	SIM
Case	ER	m_p	m_s	P_out	P_init.	T_init.	P_p	P_s	m_out	ΔP_ejector	AGR
-	1	g/s	g/s	bar	bar	K	bar	bar	g/s	mbar	%
1	4.5	0.4	1.81	1	1	220	3.95	0.960	2.21	40	
2	5	0.4	2	1	1	220	3.93	0.970	2.40	30	
3	6	0.4	2.4	1	1	220	3.93	0.977	2.80	23	46
4	7	0.4	2.8	1	1	220	3.93	0.985	3.20	15	53
5	8	0.4	3.2	1	1	220	3.93	0.994	3.60	6	60
6	9	0.4	3.4	1	1	220	3.93	1.000	3.80	0	70

The indicators used in Table 4.2 are named in Table 4.3:

Table 4.3: Explanation of indexes used in Table 4.2 [12]

R	Result of simulation
BC	Boundary Condition
IC	Initial Condition
SIM	Value coming from an other simulation

The AGR stated in the Table 4.2 is a simulation result from the SOFC AVL Matlab–Simulink model[2].

[2]Name of the model: 5kwh_concept3_AGR70new

Figure 4.15 shows the ejector layout for assigning results from the 1-D simulation results of Figure 4.4 to the correct position.

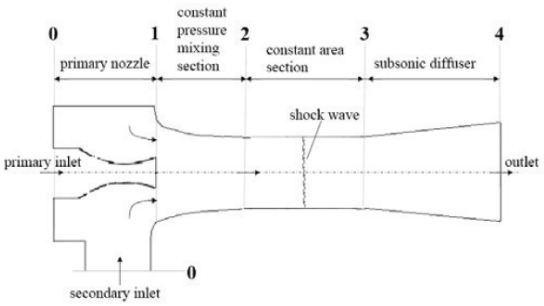

Figure 4.15: Ejector layout (**Ejector development design A**) [12]

Table 4.4: 1-D Simulation results and parameters (**Ejector development design A**) [12]

		Primary inlet	Secondary inlet	Throat nozzle	Section 1 Diffuser	Section 1 Secondary	Section 1	Section 2	Section 3	Section 4
flow rate	g/s	0.18	1.98	0.18	0.18	1.98	2.16	2.16	2.16	2.16
pressure	bar	1.90	0.96	1.03	0.58	0.58	0.58	0.58	0.45	1.02
velocity	m/s	0.00	0.00	419.32	726.20	11.80	0.00	0.00	683.26	0.00
temperature	K	298.15	907.78	257.03	174.81	622.63	0.00	500.50	443.24	547.83
diameter	mm	0.00	0.00	0.84	2.01	14.74	16.75	10.97	10.97	30.00

entrainment ratio	ER	10.99
AGR	%	70

Figure 4.16 and Figure 4.17 show the graphical represented CFD results with respect to the Mach number and the pressure. Two designs are presented, the *preliminary Design* and *final Nozzle Design 1* which is the geometric foundation for the Nozzle that was built and tested in **Ejector test system design A** and **B**.

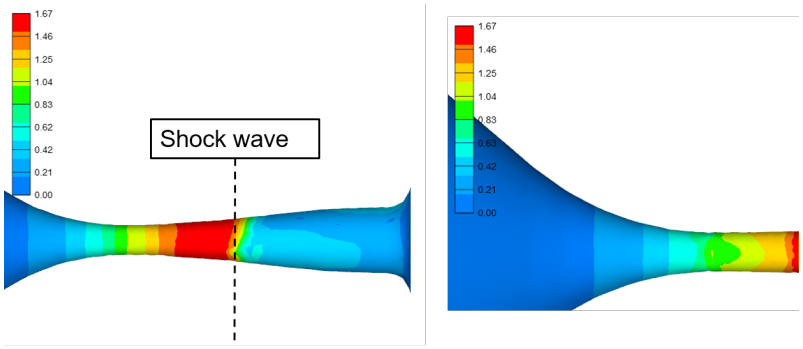

Figure 4.16: Mach-number, CFD simulation results [12]
(**Ejector development design A**)
left: preliminary Design
right: final Nozzle Design 1

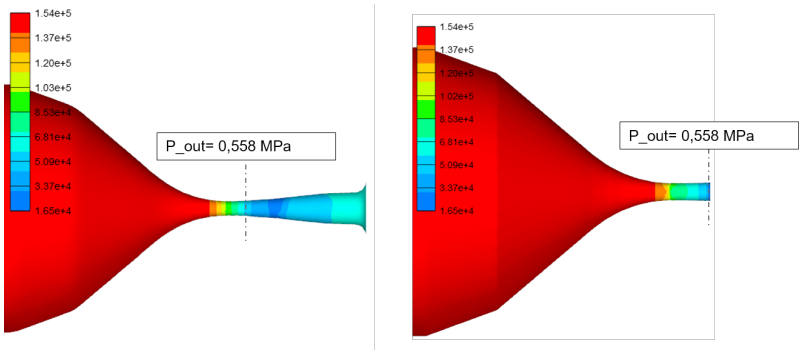

Figure 4.17: Pressure, CFD simulation results [12]
(**Ejector development design A**)
left: preliminary Design
right: final Nozzle Design 1

Because of the too long diffusor section of the nozzle, a shock wave (local pressure drop) was a result in the CFD simulations (displayed by a vertical line in Figure 4.16). A reasonable way of overcoming this problem was to change the geometry of the nozzle. M. Rossi did this by reducing the length of the diffusor (diverging part of the nozzle). The boundary condition surface therefore moved closer to point where the shockwave happened to be. This action raised concerns in the CFD department as the boundary condition should not be that close to a point of interest. Nevertheless, the nozzle was produced this way.

Finally the CFD simulation results of M. Rossi on the ejector system are presented in Figure 4.18. The results are relatively undetailed compared to the ones of M. Tkaucic. The flow distribution inside of the mixing chamber or the nozzle outlet cannot be assessed based on this graph.

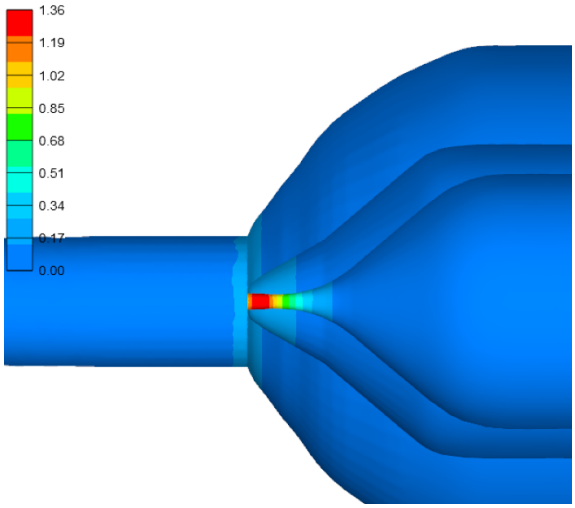

Figure 4.18: Mach number, Ejector CFD simulation results [12]
(**Ejector development design A**)

5 Experimental validation

In this chapter an overview on the basic test rig setup is given. The used sensors, methods and measurement principles are presented as well.

5.1 Preparation of testbed

This section serves as a general guidance through the measurements performed in order to make the results of further investigations comparable to the data presented in Chapter 6. The general workflow and preparations for the measurements in the fuel cell laboratory are listed here:

1. mechanically build up the test rig
2. prepare the control software (LabVIEW)
3. define zero-level on all pressure sensors (calibration)
4. define the actual ambient pressure level $p_{ambient}$ from the external sensor in the laboratory
5. apply pressure to the inlet valve via the mass flow controller and check gas tightness of the system with the aid of a leakage spray
6. close the test rig with the plastic protection walls
7. add security informations about the used gases and possible dangers referred to the test
8. calibrate venturi volume flow measurement with optimum results in the expected measurement range
9. determine the ideal position of the Laval nozzle holder (criteria: entrainment ratio)
10. investigate on performance-influencing parameters at this position of the nozzle

5.2 The laboratory test rig

In this section an overview on the ejector test rig hardware and surrounding laboratory components is given. The basic test configuration for the closed case with the possibility of heating up the system with the heat torch and an extra mass flow controller is shown in Figure 5.1.

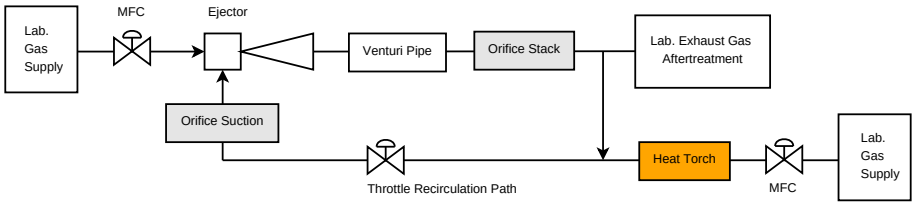

Figure 5.1: Basic test setup configuration [32]

Figure 5.2 illustrates the test rig partially assembled. The two metal flanges which are used for holding the metal orifices, the pressure sensors and the Venturi pipe are shown in this figure. The primary inlet is on the left side and the output on the right one.

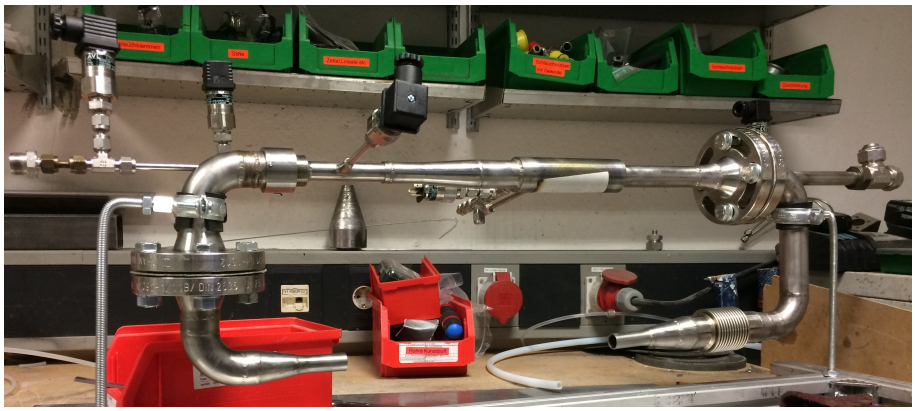

Figure 5.2: Laboratory preparation of test rig for the open case
(**Ejector test system design A**)

The laboratory setup in Figure 5.3 needed to be adapted before using it for the hot closed case testing. The electrical heater was planned to be inside of the recirculation path, but this was not possible because the electrical heater can only be supplied with gases up to 120 °C. The maximum measured gas output temperature of the electrical heater during the operation was 704 °C.

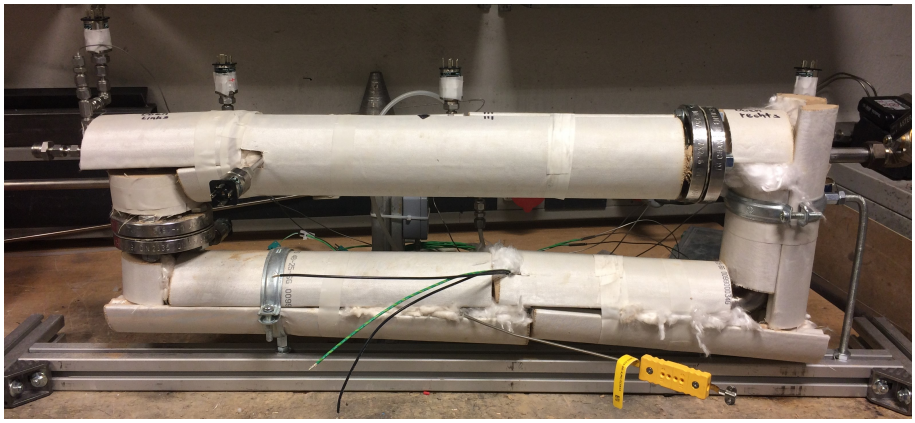

Figure 5.3: Laboratory preparation of test rig for the closed case
(**Ejector test system design A**)

In Figure 5.4 and 5.5 the test rig for the closed case is represented. All the relevant components are listed and a representative ejector image is added to indicate its location in the test rig. The secondary mass flow is calculated by subtracting the primary mass flow (value from the mass flow controller) from the mass flow through the Venturi pipe.

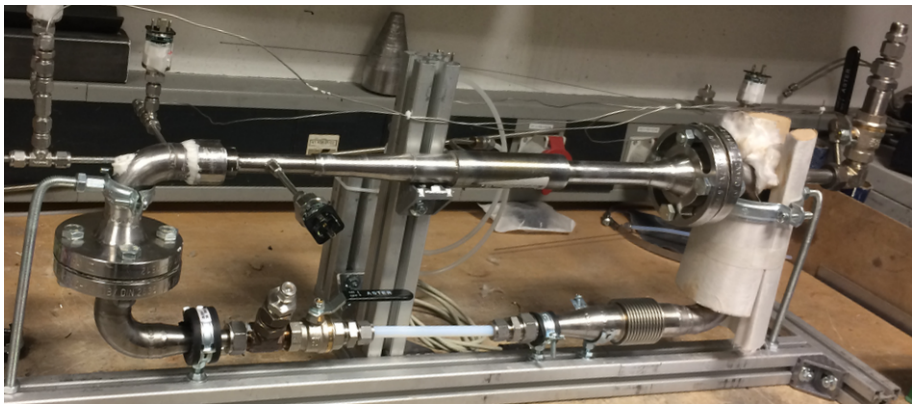

Figure 5.4: Laboratory preparation of test rig for the closed case
(**Ejector test system design A**)

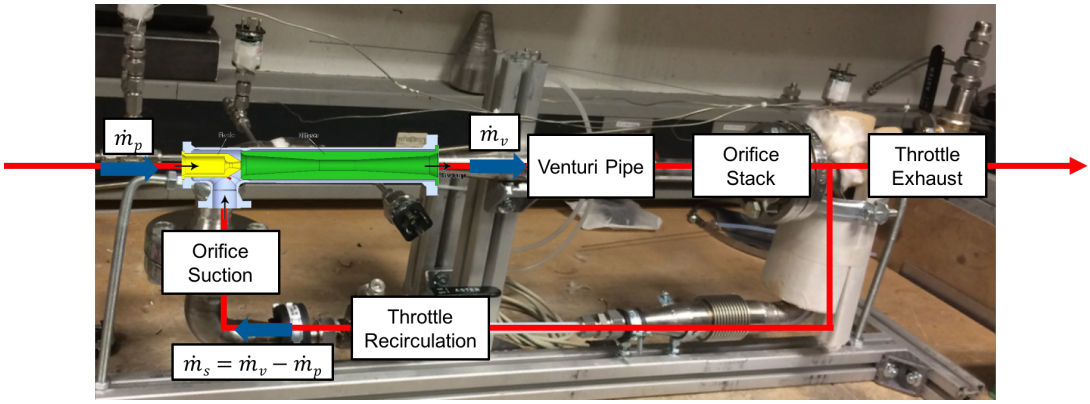

Figure 5.5: Laboratory preparation of test rig for the closed case including description
(**Ejector test system design A**)

The setup in Figure 5.6 shows the closed rig with the electrical heater in the adapted correct position. For the operation the test rig was fully insulated. The compensator is needed to cope with thermal expansions and the difference in length coming from the change of distance between the mixing chamber and the nozzle.

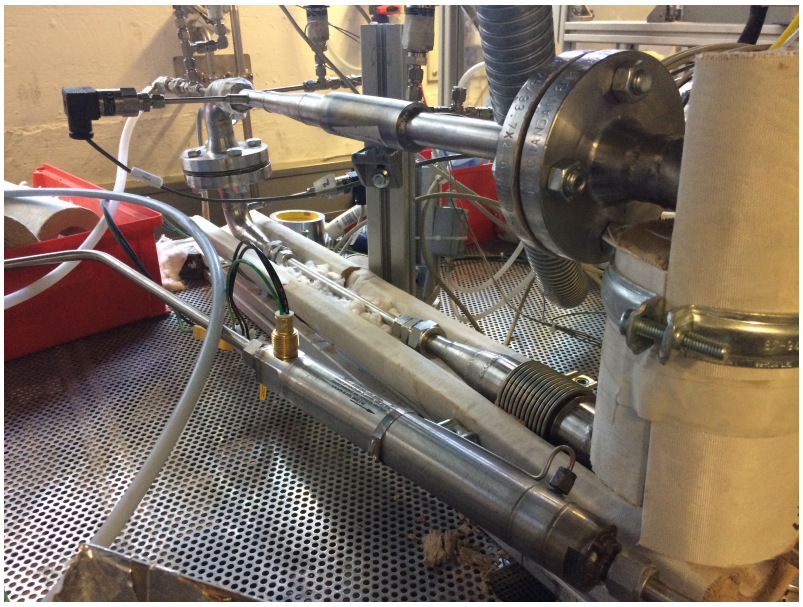

Figure 5.6: Laboratory test rig with electrical heater
(**Ejector test system design A**)

Figure 5.7 depicts the high-temperature sealing and the *Orifice Suction* with a diameter of $d_s = 9.6\,\text{mm}$. This metal orifice was needed to analyze the ejector behavior at a pressure loss in the respective anode path for the hot case.

Figure 5.7: *Orifice Suction* with flange and high-temperature sealing

Figure 5.8 shows a manufacture error on the transition between the nozzle holder cone and the nozzle itself. The actual position (and the length) of the nozzle was correct but the angle of the cone was wrong. In Figure 5.9 the nozzle is brought into the position where the step disappears. The effect of this error was analyzed and the influence is described in Chapter 6.2.1.

Figure 5.8: Nozzle-holder with step: **POS1** and **POS2** (**Ejector test system design A**)

Figure 5.9: Nozzle-holder without step: **POS3** (**Ejector test system design A**)

The user interface for controlling the test rig via the software LabVIEW is displayed in Figure 5.10. The control palettes for the mass flow controllers are on the top and are named „AIR2 (5000 Nl/h)“ and „CH4 (3000 Nl/h)“. The value in the brackets is the maximum possible volume flow on the respective line.

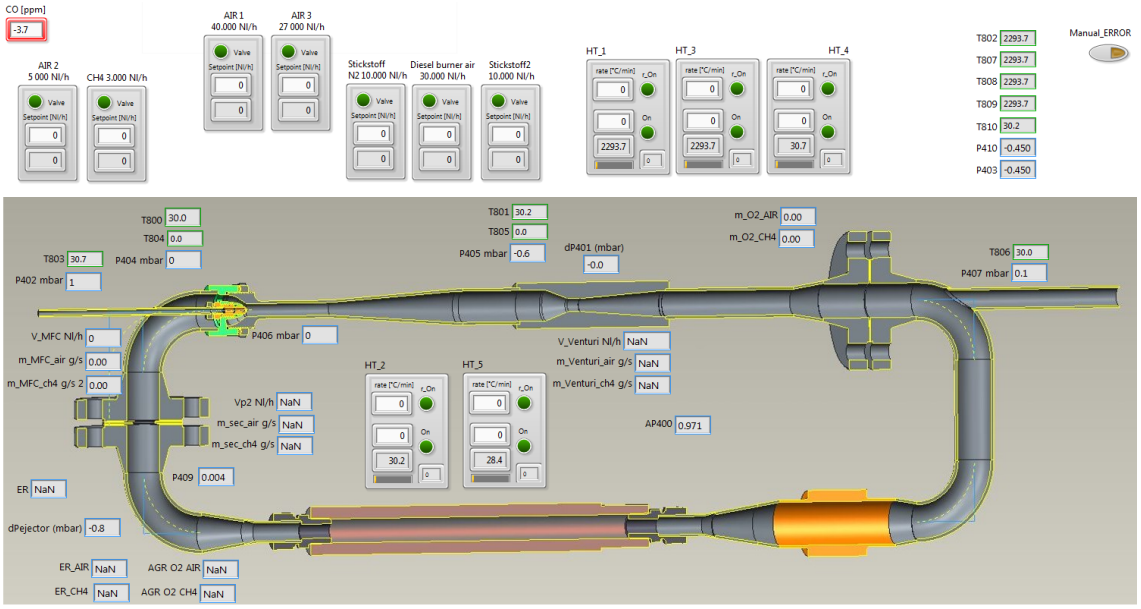

Figure 5.10: LabVIEW test rig software user interface

Figure 5.11 is focusing on the position and naming of the relevant pressure and temperature sensors for the measurements. As already stated, the electrical heater is attached as shown in Figure 5.1 and not how it is displayed here. Table 5.1 gives the details of relevant sensors and physical quantities.

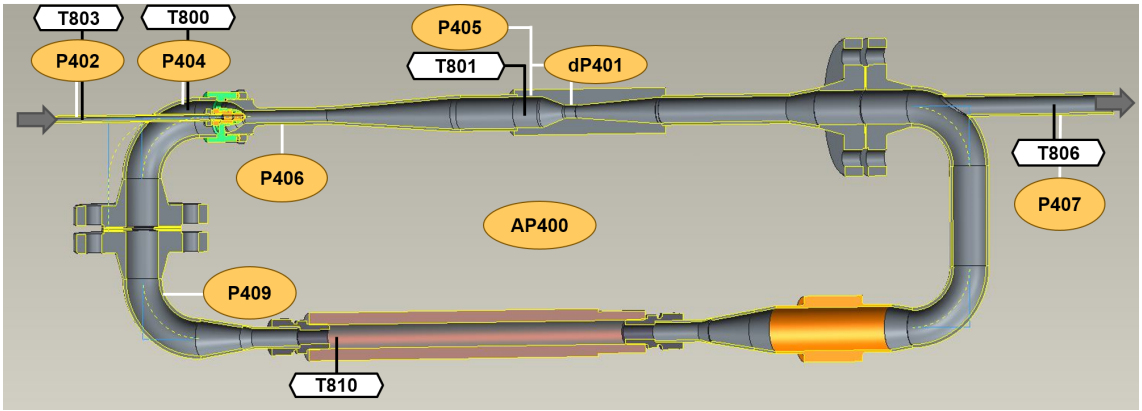

Figure 5.11: Test rig pressure and temperature sensor locations

Table 5.1: General nomenclature description

Name	Unit	Description	Measurement range
$AP400$	mbar	ambient pressure	
$dP401$	mbar	Venturi differential pressure	$(0\,\text{mbar} \ldots +20\,\text{mbar})$
$P402$ (P_M)	mbar	primary inlet (motive) pressure	$(-6\,\text{bar} \ldots +6\,\text{bar})$
$P404$ (P_E)	mbar	secondary inlet (suction) pressure	$(-0.3\,\text{bar} \ldots +0.3\,\text{bar})$
$P405$ (P_D)	mbar	Venturi inlet pressure	$(-0.3\,\text{bar} \ldots +0.3\,\text{bar})$
$P406$	mbar	mixing chamber pressure	$(-0.3\,\text{bar} \ldots +0.3\,\text{bar})$
$P407$	mbar	test rig outlet pressure	$(-0.3\,\text{bar} \ldots +0.3\,\text{bar})$
$P409$	mbar	secondary inlet pressure before orifice	$(-0.3\,\text{bar} \ldots +0.3\,\text{bar})$
$T800$ (T_E)	°C	secondary inlet (suction) temperature	
$T801$ (T_D)	°C	Venturi gas temperature	
$T803$ (T_M)	°C	primary inlet (motive) temperature	
$T806$	°C	test rig outlet temperature	
$T810$	°C	heat torch temperature	
$\dot{V}_p$	Nl/h	primary volume flow	
$\dot{V}_s$	Nl/h	secondary volume flow	
$\dot{V}_v$	Nl/h	volume flow at Venturi pipe	
$\dot{m}_p$	g/s	primary mass flow	
$\dot{m}_s$	g/s	secondary mass flow	
$\dot{m}_v$	g/s	mass flow at Venturi pipe	

5.3 Instrumentation and measurements

For all the measurements a program based on a LabVIEW software and a National Instruments realtime IO was used. For the communication with the mass flow controllers the same tools were used.

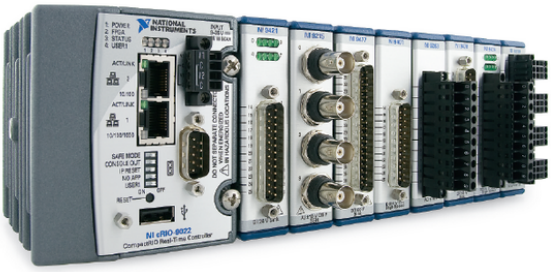

Figure 5.12: National Instruments cRIO [33]

5.3.1 Pressure measurement

All the pressure sensors used in the setup are measuring the relative pressure with respect to the local ambient pressure. Before starting the measurements, all the sensors connected to the control software need a zero adjustment. Meaning that an existing offset in the pressure measurement is being erased. The ambient pressure was measured inside of the fuel cell test rig once each day compared to the real-time measurement of all other signals. This value was entered into the LabVIEW control software manually.

$$P_{absolute} = P_{atmosphere} + P_{gauge} \tag{5.1}$$

Figure 5.13 shows the difference between measuring the absolute pressure either or the relative pressure with reference to the ambient pressure of the atmosphere. A shift of the ambient pressure will not be visible when measuring the relative pressure.

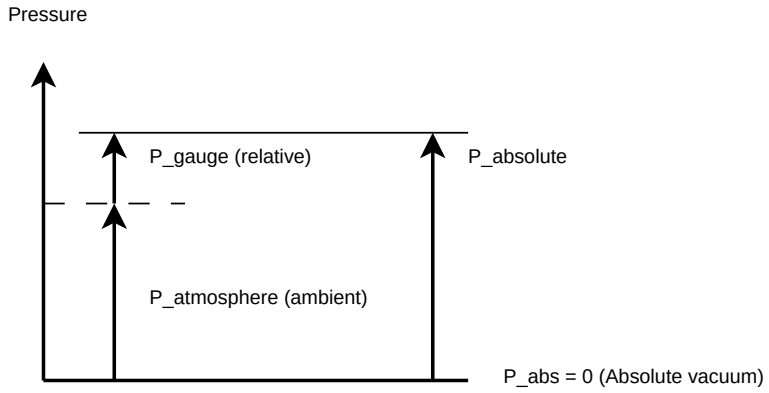

Figure 5.13: Visualization of pressure levels

5.3.2 Temperature measurement

All the temperature sensors are set in the middle of each point of interest in order to measure the gas temperature and reduce the influence from the surrounding material. This was realized by pushing in the temperature sensor to the maximum (reaching the opposite side of the pipe's wall) and pulling it out half of the pipe's-diameter. All of the used sensors were of the type K. It is important to consider the appropriate polarity in order to get correct results. Especially at the swagelok fittings for the temperature sensors the gas tightness fo the system has to be checked precisely as this is a common error source.

5.3.3 Mass flow controller

A mass flow controller is a device that regulates the a gas- or liquid flow in order to reach a defined amount of mass per time passing through a pipe. An

exemplary internal block diagram is shown in Figure 5.14. The mass flow meter (MFM) represents the measuring element which sends the actual value to the controller. There according to the setpoint value a control quantity is evaluated depending the controller method and parameters. This control quantity is then send to the proportional valve which influences the mass flow in the appropriate way.

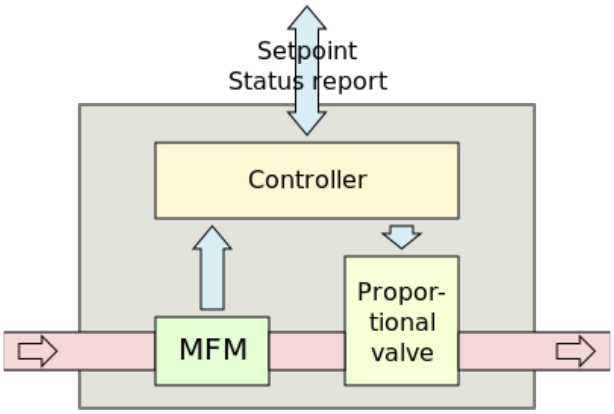

Figure 5.14: Mass Flow Controller (MFC) internal block diagram [34]

5.3.4 Volume flow measurement

The base for all flow regime comparisons of the CFD simulation results to the experimental data are the values coming from the mass flow controllers and the volume flow measurement inside of the ejector system. Therefore, this measurement is a crucial element of the test rig. The principle is based on the Venturi effect:

> *„In fluid dynamics, an incompressible fluid's velocity must increase as it passes through a constriction in accord with the principle of mass continuity, while its static pressure must decrease in accord with the principle of conservation of mechanical energy.“* [35]

The theoretical pressure drop at the constriction shown in Figure 5.15 is given by the Bernoulli equation for a steady, incompressible and inviscid flow [35]:

$$p_1 - p_2 = \frac{\rho}{2}(v_2^2 - v_1^2) \tag{5.2}$$

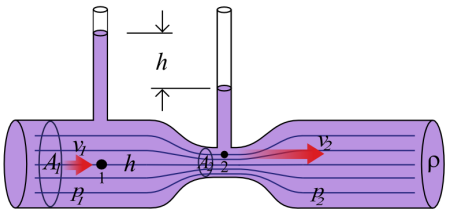

Figure 5.15: Visualization of the Venturi effect [36]

The construction drawing for the used Venturi pipe is shown in Figure 5.16. The pipe diameter at the gas inlet section is d_2 and the diameter of the constricted area is d_1. The measurement range of this specific Venturi pipe is limited to 20.000 Nl/h resulting in a differential pressure of nearly 20 mbar.

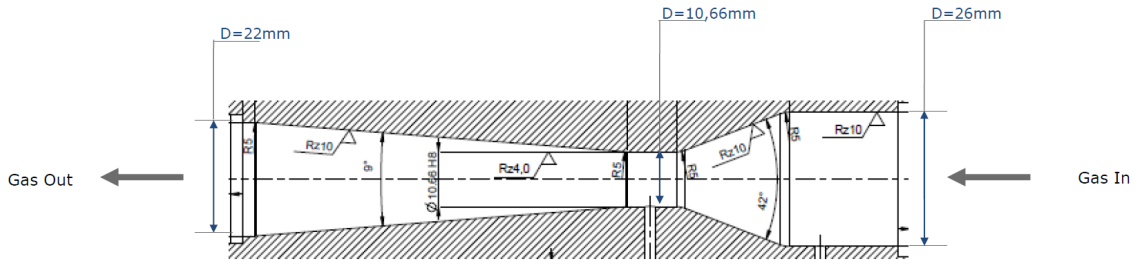

Figure 5.16: Venturi construction drawing [37]
$d_1 = 10.66\,\text{mm}$, $d_2 = 26\,\text{mm}$

In order to calculate the density ρ_1 of the streaming gas, the static pressure p_1 and the temperature T_1 at the entrance of the Venturi pipe have to be measured.

$$\rho_1 = m_{gas} \frac{T_N p_1}{p_N V_N T_1} \tag{5.3}$$

$$\dot{V}_1 = \frac{\pi}{4} \frac{{d_1}^2}{\sqrt{\left(\frac{d_1}{d_2}\right)^4 - 1}} \sqrt{\frac{2\Delta p}{\rho_1}} = \alpha \sqrt{\frac{2\Delta p_1}{\rho_1}} \tag{5.4}$$

As shown in Figure 5.11 the variables used in formula (5.3) and (5.4) are represented as follows: $p_1 = P405$ and $T_1 = T801$ as wells as $\Delta p = dP401$. It is also shown in Table 5.2 where the used variables are described.

Table 5.2: Nomenclature definition for volume flow calculations

$\Delta p = dP401$	Pa	Differential pressure
ρ	$\frac{kg}{m^3}$	Density at inlet
d_1	m	Diameter at Venturi inlet
d_2	m	Diameter at Venturi nozzle
$p_1 = P405$	Pa	Absolute pressure at Venturi inlet
$\dot{V}_1$	$\frac{m^3}{s}$	Volume flow at Venturi inlet
$T_1 = T801$	K	Temperature at Venturi inlet
$\dot{V}_N$	$\frac{Nl}{h}$	Standard volume flow
m_{Gas}	kg	Mass of the gas
T_N	K	Standard temperature (273.15 K)
p_N	Pa	Standard pressure ($1.01325 \cdot 10^5$ Pa)

5.3.5 Calibration of volume flow measurement

In order to reach good calibration results in the range of the expected measurement results, the setup of the test rig needed to be changed. This was because the volume flow through the nozzle was at it's maximum at around 2200 Nl/h for the use with air. Therefore, the secondary inlet was connected to a mass flow controller to reach higher volume flows through the Venturi pipe as shown in Figure 5.17 .

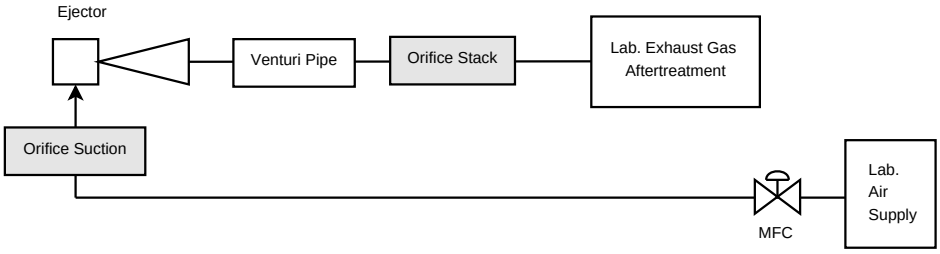

Figure 5.17: Test setup for the calibration of the Venturi pipe

Assuming an entrainment ratio of $ER = 10$ and a variable primary inlet volume flow $\dot{V}_{p,air}$ the resulting flow through the Venturi pipe is:

$$\dot{V}_{v,air} = \dot{V}_{p,air} + \dot{V}_{s,air} = \dot{V}_{p,air} + ER \cdot \dot{V}_{p,air} \tag{5.5}$$

$$\dot{V}_{v,air} = (1 + 10) \cdot \dot{V}_{p,air} = 11 \cdot \dot{V}_{p,air} \tag{5.6}$$

Assuming a primary inlet volume flow variation from 360 to 1124 Nl/h the expected range of the volume flow through the Venturi pipe is:

$$\dot{V}_{v,air} = 11 \cdot 360\,\text{Nl/h} = 3960\,\text{Nl/h} \tag{5.7}$$

$$\dot{V}_{v,air} = 11 \cdot 1124\,\text{Nl/h} = 12364\,\text{Nl/h} \tag{5.8}$$

Therefore, the aim is to have relation of $\dot{V}_{s,air}/\dot{V}_{v,air} = 1$ in the calibration mode of the Venturi pipe as in Figure 5.17. In Figure 5.18 the original and the calibrated ratio is shown using the constant correction factor f_0.

$$\dot{V}_{s,air}/\dot{V}_{v,air}\ \text{calibrated} = f_0 \cdot \dot{V}_{s,air}/\dot{V}_{v,air}\ \text{original} \tag{5.9}$$

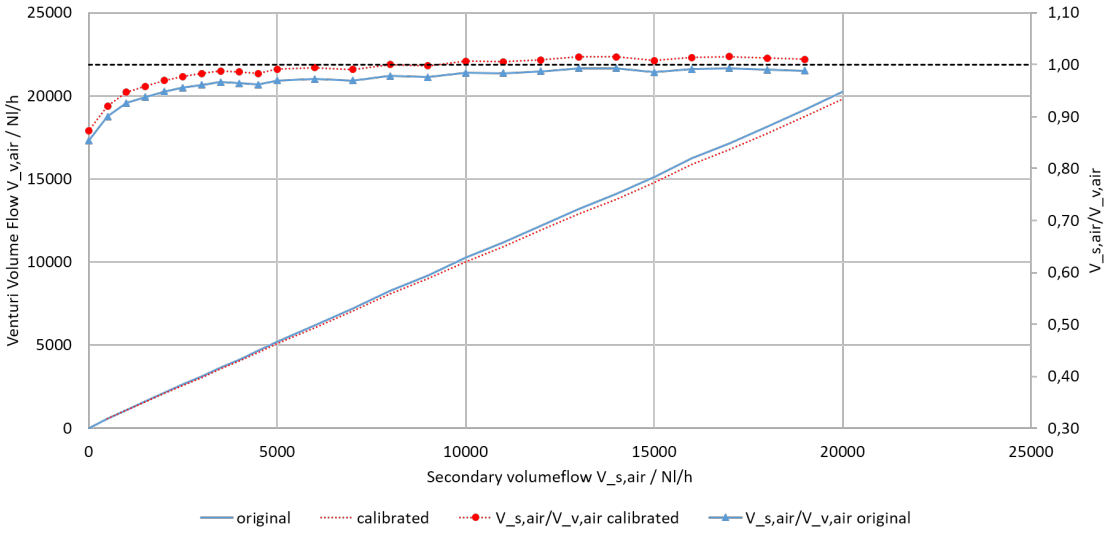

Figure 5.18: Chart for the calibration of the Venturi pipe

6 Test and CFD results

This chapter deals with all the results gained during the time of the thesis. First of all the **Ejector test system design A** was analyzed followed by the **Ejector test system design B**. Afterwards a comparison of both systems is presented. At the end of this chapter the results of the CFD simulations from M. Tkaucic regarding the real test system (**Ejector test system design A**) are presented and compared to the data gained from the measurements.

6.1 Operating points

In order to operate the fuel cell system not only in full-load condition but also in part-load, the amount of methane as fuel is modifiable. Therefore, the operation of the ejector system was analyzed in different operating ranges as well. The entrainment ratio however, should stay the same for all operating points. The values for the operating points are stated in Table 6.1.

Table 6.1: Operating points of the ejector system

$\dot{m}_p$	$\dot{m}_p$	$\dot{V}_{p,air}$	$\dot{V}_{p,methane}$
g/s	g/h	Nl/h (79% N2 / 21% O2)	Nl/h (100% CH_4)
0.1	360	280	504
0.2	720	560	1009
0.3	1080	840	1513
0.4	1440	1120	2017

The equation (6.1) shows the conversion from primary mass flow to primary volume flow with using the gas density at standard conditions[3] for air[4]. The equation is also valid for using methane[5].

$$\dot{m}_p \text{ (g/s)} = \dot{V}_{p,air} \cdot \frac{\rho_{N,air}}{3600} \text{ (Nl/h)} \tag{6.1}$$

[3]Standard conditions: ($p_N = 1013.25$ bar and $T_N = 273.15$ K) [17]
[4]$\rho_{N,air} = 1.293$ kg/m^3 [38]
[5]$\rho_{N,methane} = 0.717$ kg/m^3 [39]

6.2 Ejector test system design A

In this section all the measurement results with respect to the **Ejector test system design A** are described. The basic design informations are stated in Figure 6.1:

Nozzle 1: Nozzle throat diameter $d_T = 0.8\,\text{mm}$
Nozzle 1: Nozzle exit diameter $d_{NE} = 0.87\,\text{mm}$
Ejector 1: Mixing chamber diameter $d_c = 10.5\,\text{mm}$
Ejector 1: Mixing chamber length $l_c = 70.4\,\text{mm}$
Position: $x_0 + \Delta x$

Figure 6.1: Main design parameters of **Ejector test system design A** [12]

6.2.1 Parameter: Three nozzle/nozzle holder positions

The position of the nozzle with respect to the mixing chamber is a crucial performance parameter for the operation of the ejector. The measurements are carried out at four different operating points (Table 6.1) for each of the three nozzle holder positions (Figure 6.3).

Measurement procedure for nozzle holder position **POS1**:
1) Open throttle recirculation path
2) Set primary volume flow to $\dot{V}_{p,air} = 280\,\text{Nl/h}$
3) Start recording measurement values (1 s for each point)
4) Close throttle recirculation path ($\approx 60\,\text{s}$)
The steps 1) to 4) are repeated but with different volume flows. Then the position of the nozzle holder is changed and the whole measurement is repeated.

With the throttle open the entrainment ratio is high as the air flow can circulate through the system with comparably small friction losses. The throttle closing leads to an increased pressure loss in this section of the system and a decrease of the entrainment ratio as shown in Figure 6.5. The maximum achievable discharge suction pressure ($dP_{ejector}$) can be found at an entrainment ratio of zero.

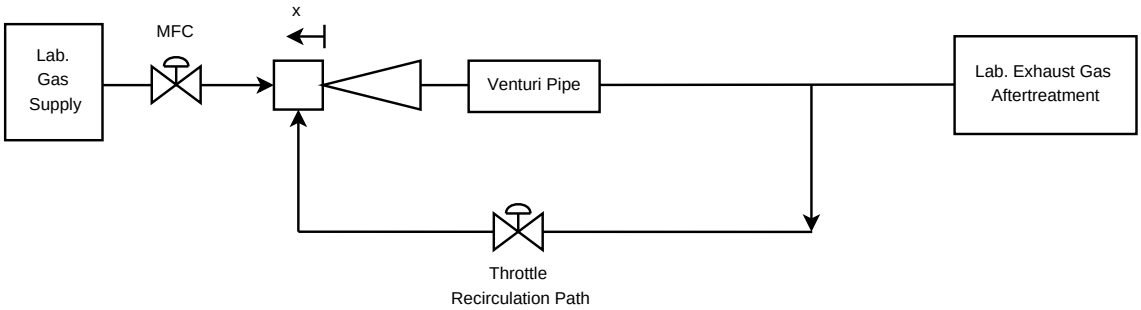

Figure 6.2: Test setup for parameter: Nozzle holder position

The three different positions which are shown in Figure 6.3 are described here:

POS1 (green)
This is the original design position with a step between the nozzle holder and the nozzle itself as shown in Figure 5.8.

POS2 (orange)
In this position the distance between the nozzle holder and the mixing chamber is at its maximum and the step is still existent as in position POS1.

POS3 (blue)
Compared to position POS2 the step is removed by moving the nozzle further backwards with reference to the nozzle holder. An image of this status is shown in Figure 5.9. The position of the holder is unchanged compared to POS2.

Figure 6.3: Position variation of the nozzle and the nozzle holder (**POS3**, **POS2**, **POS1**) from left to right

Figure 6.4 shows the inner thread between the nozzle and nozzle holder and the outer thread between the nozzle holder and mixing chamber. Those two threads are used the position variations shown in Figure 6.3.

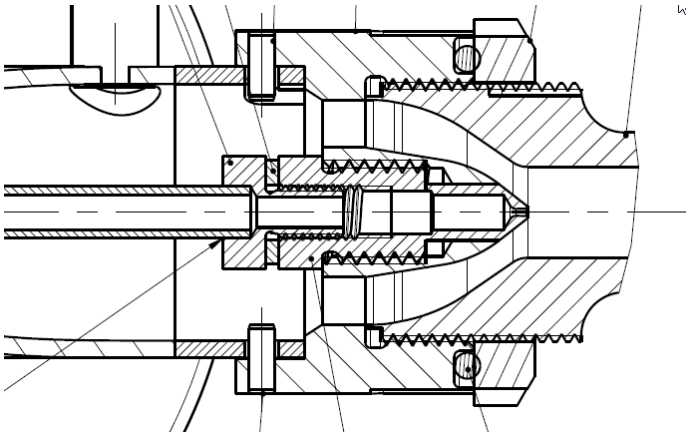

Figure 6.4: Construction drawing with Laval nozzle (**Ejector development design A**) [40]

[5]Christopher Sallai, AVL/AT Fuel Cell Department PTE-DRF [14.02.2017]

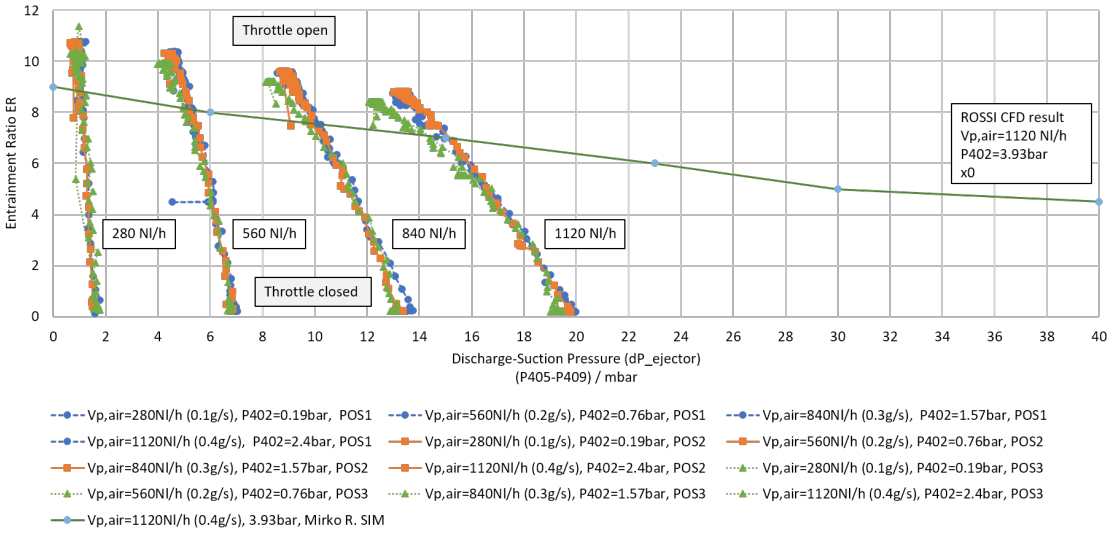

Figure 6.5: Parameter: Nozzle and nozzle holder position and throttle recirculation path
Design position x_0 and $\Delta x = 0\,\text{mm}$
$\dot{V}_{p,air} = 1120\,\text{Nl/h}$
Ejector test system design A
06.04.2017

The Figure 6.5 shows measurement as well as the simulation results by M. Rossi described in Section 4.7. In fact it can be said that the CFD simulation of M. Rossi is hardly comparable to the results from measurements. He neglected the friction between air and the walls of his CFD design which is very likely the reason for the big difference. The change between the positions mentioned in Figure 6.3 is very small. Possible reasons for this phenomena are explained in chapter 6.2.2.

6.2.2 Parameter: Four nozzle holder positions

In Section 6.2.1 three positions regarding the nozzle and nozzle holder are analyzed to get a good understanding of the performance influence of this parameter. In the following experiment measurements were repeated and an extra position was added to look at the difference between positions more in detail. The test setup is unchanged and shown in Figure 6.2. The so called design position x_0 refers to the position **POS1** where the distance between the nozzle and the mixing chamber is at its minimum. The outer thread is completely tightened and the step between nozzle and its holder is existent. This experiment is carried out at two different primary volume flows. The higher primary flow of 1700 Nl/h was used because the change in performance is more clearly visible compared to low volume flows.

The variation of the nozzle holder shows a relative increase of the entrainment ratio of 3.9% at the position x_3 compared to the design position x_0. There are two ways of explaining this fact. On one hand the CFD simulations of M. Tkaucic of the real test ejector system setup show that the mixing chamber diameter is too

high. This results in early turbulences in the mixing area meaning a loss of kinetic energy. On the other hand, positioning of the nozzle with respect to the mixing chamber is not ideal. The simulations suggest a position further away from the mixing chamber, so that the expanding beam coming from the outlet of the nozzle is hitting the mixing chamber having the same cross section. An empirical test on the open test rig without the nozzle holder has also shown that an increase of the ejector performance for **Ejector test system design A** is possible by increasing the distance between the nozzle and mixing chamber even further. The optimum operating position as well as the mixing chamber diameter have to be investigated precisely in the CFD simulations to enable design improvements.

The graph in Figure 6.6 depicts the change of the entrainment ratio with the variation of distance from the design position x_0. The throttle in the recirculation path is open for all these measurement points.

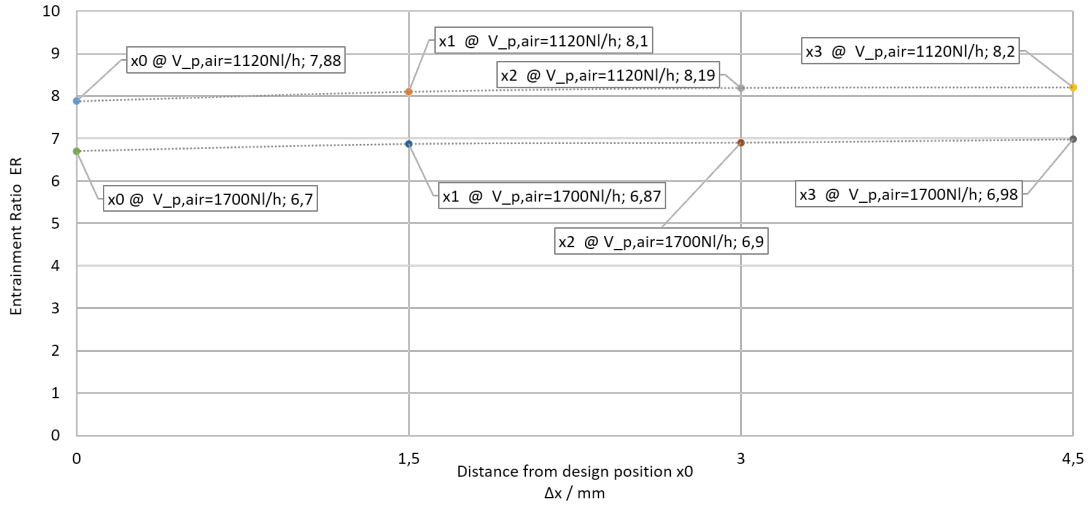

Figure 6.6: Parameter: Nozzle holder position
Design position x_0 with $\Delta x = 0\,\text{mm}$
Ejector test system design A

In Table 6.2 the relative change of the nozzle holder to the design position x_0 is shown. The Table contains measurements results for two different primary inlet pressures.

Table 6.2: Position variation of the nozzle holder (**Ejector test system design A**)

Position Name	Δx	ER	$\dot{V}_{p,air}$	$\dot{V}_{s,air}$	$\frac{ER_{max}-ER}{ER_{max}}$	$P402$
-	mm	1	Nl/h	Nl/h	%	bar
x_0	0	7.88	1120	8826	3.90	2.38
x_1	1.5	8.1	1120	9072	1.22	2.38
x_2	3	8.19	1120	9173	0.12	2.38
x_3	4.5	8.2	1120	9184	0.00	2.38
x_0	0	6.7	1700	11390	4.01	4.07
x_1	1.5	6.87	1700	11679	1.58	4.07
x_2	3	6.9	1700	11730	1.15	4.07
x_3	4.5	6.98	1700	11866	0.00	4.07

The graphs in Figure 6.7 and Figure 6.8 also show the change of the entrainment ratio. But compared to the measurement data in Figure 6.6 with increasing the system pressure loss through closing the recirculation path throttle.

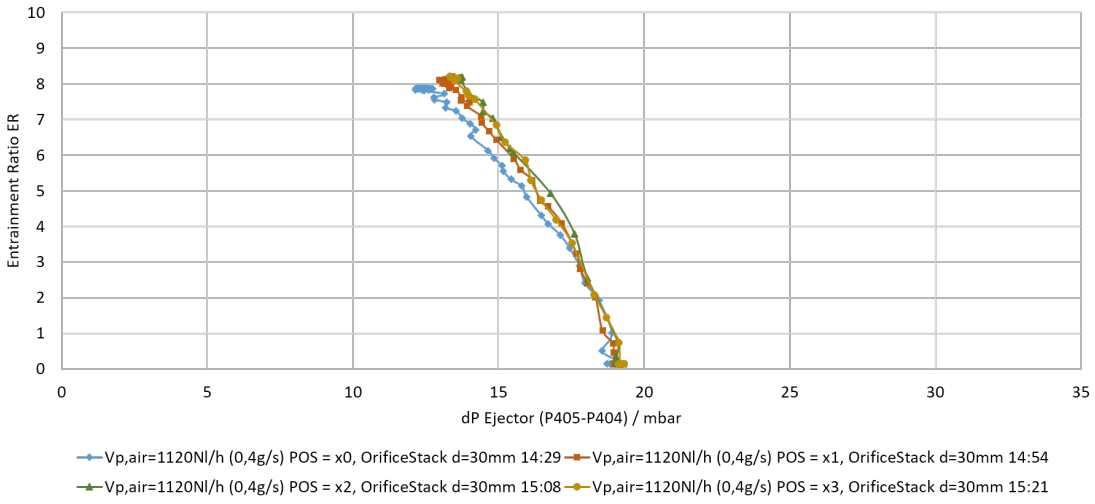

Figure 6.7: Parameter: Four nozzle holder positions
Design position x_0
$\dot{V}_{p,air} = 1120\,\mathrm{Nl/h}$
Orifice Stack diameter $d_s = 30\,\mathrm{mm}$
Ejector test system design A
20.04.2017

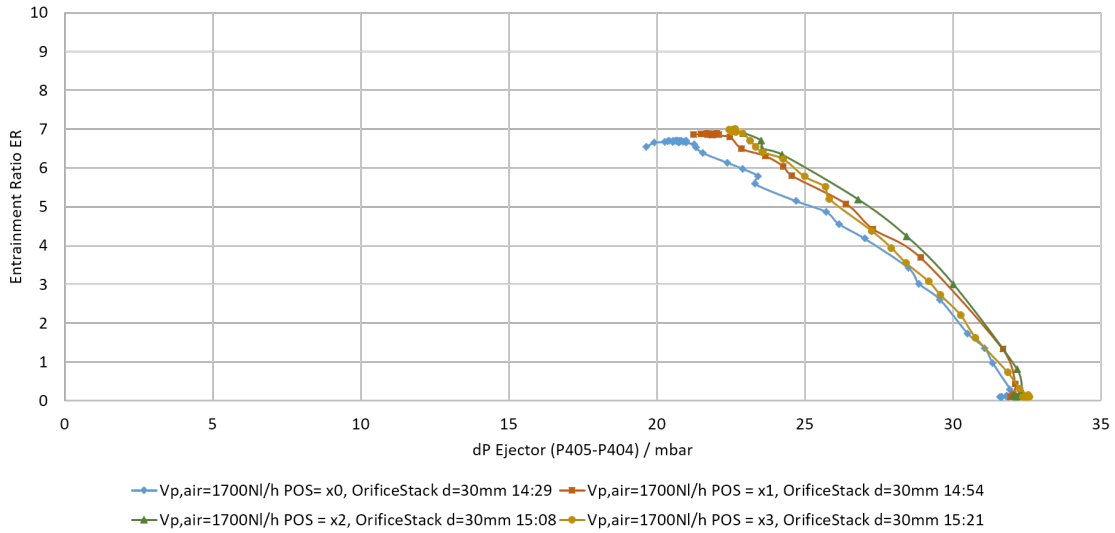

Figure 6.8: Parameter: Four nozzle holder positions
Design position x_0
$\dot{V}_{p,air} = 1700\,\mathrm{Nl/h}$
Orifice Stack diameter $d_s = 30\,\mathrm{mm}$
Ejector test system design A
20.04.2017

6.2.3 Parameter: Pressure loss through orifice

In this section the influence of a pressure loss through an orifice on the representative anode line or the recirculation line is evaluated. This is especially important as the entrainment ratio is highly dependent on the existing pressure difference over the ejector. The test setup scheme for this experiment shown in Figure 6.9 is enhanced by the terms *Orifice Suction* and *Orifice Stack*. Whereas the pressure loss in the recirculation path is realized by the throttle and not the available *Orifice Suction*. This was needed to cut measurement time as replacing the orifice is time-consuming.

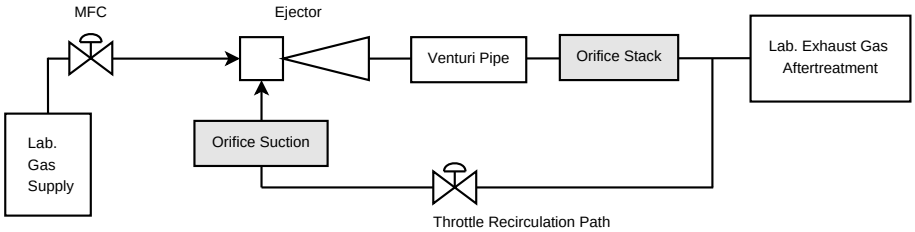

Figure 6.9: Test setup configuration for the pressure loss through orifice measurement

The results in Figure 6.10 show that it does not change the general behavior of the ejector if the pressure drop appears on the representative anode path (*Orifice Stack*) or in the recirculation path (*Orifice Suction*). Because of the different volume flows in each path one orifice results in different pressure drop depending on

the position in the system. A diameter of *Orifice Stack* $d_s = 30\,\text{mm}$ means that no orifice is being used at all. It is only stated for comparison reasons.

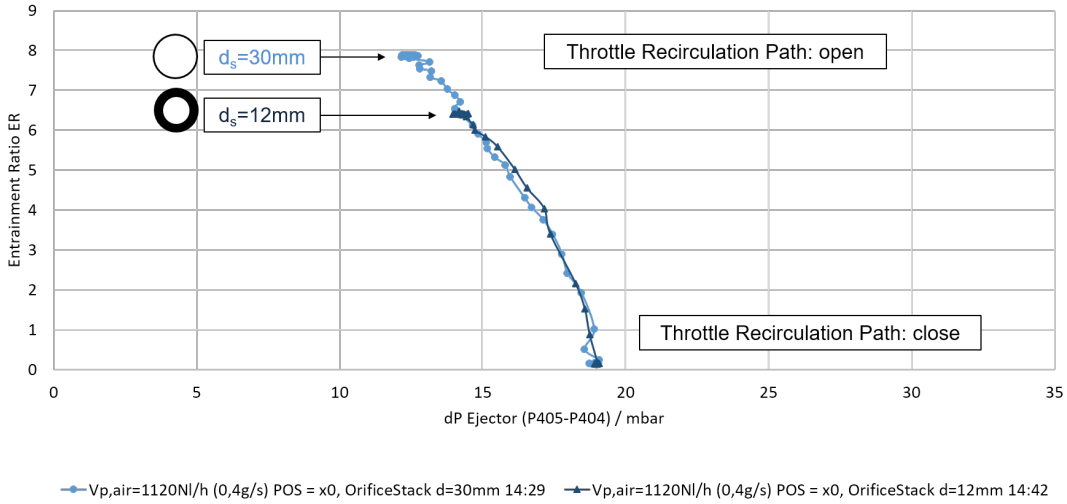

Figure 6.10: The effect of orifices in the system representing a pressure loss through friction
d_s . . . Diameter of Orifice Stack
Ejector test system design A

6.2.4 Parameter: Input pressure variation

The relation between the motive pressure and the primary volume flow is not linear for low volume flow rates. No orifices are built into the system for this parameter analysis. The results of this experiment are in line with expectations.

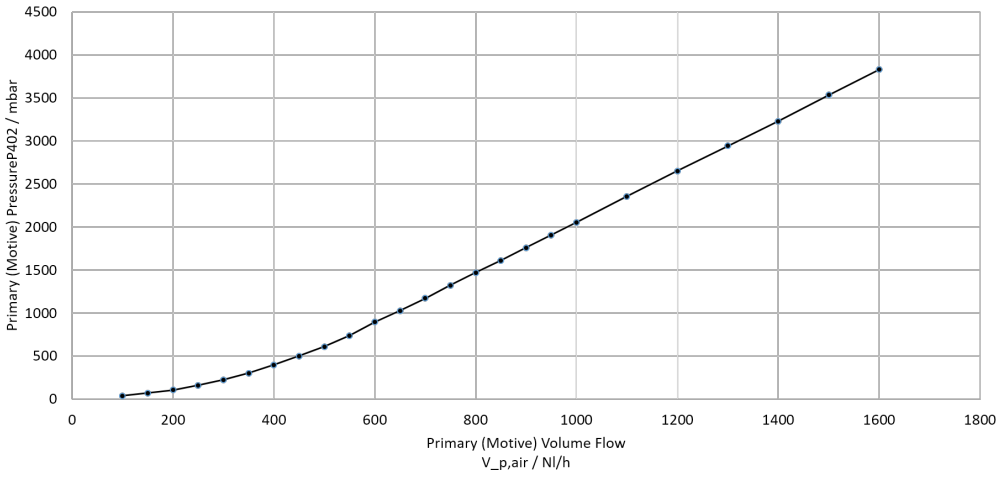

Figure 6.11: Motive Pressure vs. Primary Volume Flow
$\dot{V}_{p,air} = 1120\,\text{Nl/h}$
$T800 = 26\,^{\circ}\text{C}$
$T803 = 26\,^{\circ}\text{C}$
Ejector test system design A

6.2.5 Parameter: System pressure level

The influence of pressurizing the ejector system is analyzed in this section. Therefore, the component *Throttle Exhaust* is brought into the exhaust line. By gradually closing this throttle, the pressure inside of the system in increasing as it is connected to primary inlet pipe coming from the mass flow controller. The experiment was carried out at a primary volume flow of 1000 Nl/h. The test setup is shown in Figure 6.12. The throttle in the recirculation path and the orifices were not used here.

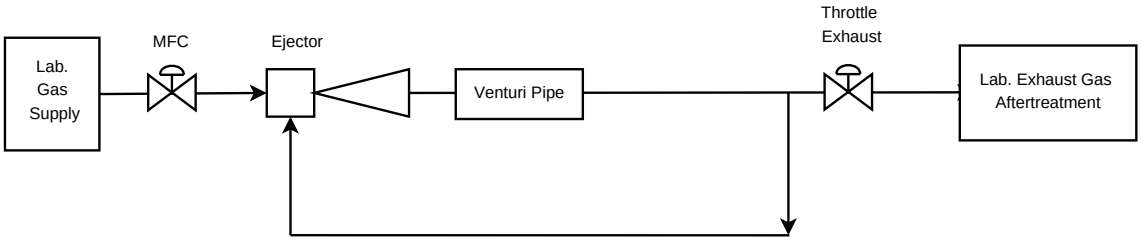

Figure 6.12: Test setup for parameter: System pressure level

Figure 6.13 shows the measurement data regarding the influence of the test rig outlet pressure $P407$ (directly before the throttle exhaust) on the entrainment ratio. The reduction of the entrainment ratio as the system pressure level is being increased is relatively low. Therefore, it can be said that looking at the real operating case of the ejector, the system pressure can be neglected as it is in the area of the ambient pressure. In order not to damage the system's sealings because of a too high overpressure regarding to the absolute ambient air pressure, the increase was stopped at $P407 = 370\,\text{mbar}$.

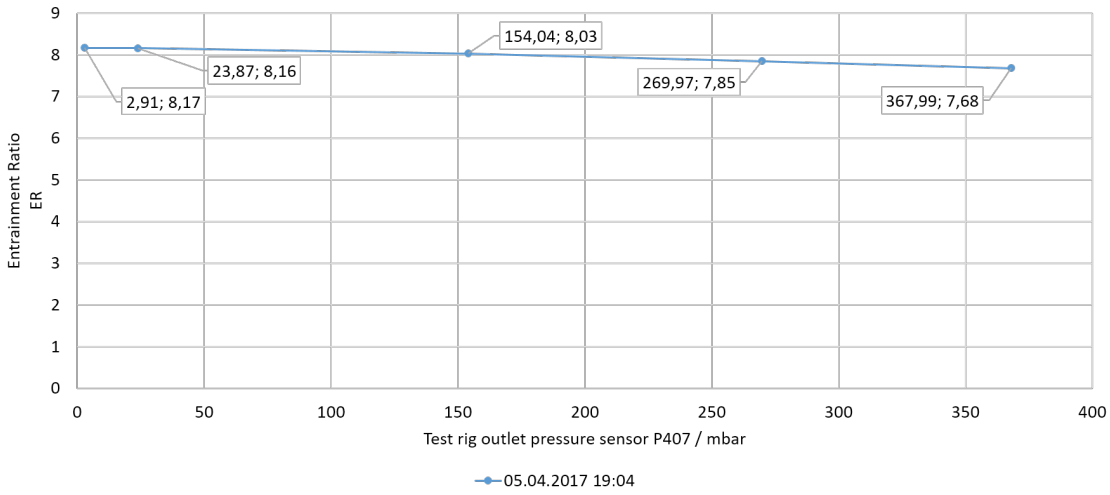

Figure 6.13: Parameter: System pressure level (choked exhaust)
$T803 = 26\,°\text{C}$
$T804 = 26\,°\text{C}$
$\dot{V}_{p,air} = 1000\,\text{Nl/h}$
05.04.2017 19:04

Table 6.3: System Pressure Level Variation

Index	ER	$\dot{V}_{p,air}$	$\dot{V}_{s,air}$	$P407$	$\frac{ER_{max}-ER}{ER_{max}}$
-	1	Nl/h	Nl/h	mbar	%
1	8.17	1000	8170	2.91	0.0
2	8.16	1000	8160	23.87	0.1
3	8.03	1000	8030	154.04	1.7
4	7.85	1000	7850	269.97	3.9
5	7.68	1000	7680	367.99	6.0

6.2.6 Parameter: System temperature

The fuel cell system anode off gas temperature in the real setup is around 620 °C. Therefore, the system temperature is a crucial parameter for the operation of the ejector system. For heating up the system the primary inlet volume flow was kept at $\dot{V}_{p,air} = 1000\,\mathrm{Nl/h}$ in order to create a recirculation in the test setup in order to create an even temperature distribution. The heat torch was operated at $\dot{V}_{HT,air} = 10000\,\mathrm{Nl/h}$ in order to allow the maximum available heating power to be applied to the heater. This leads to a electrical heater outlet temperature of 700 °C.

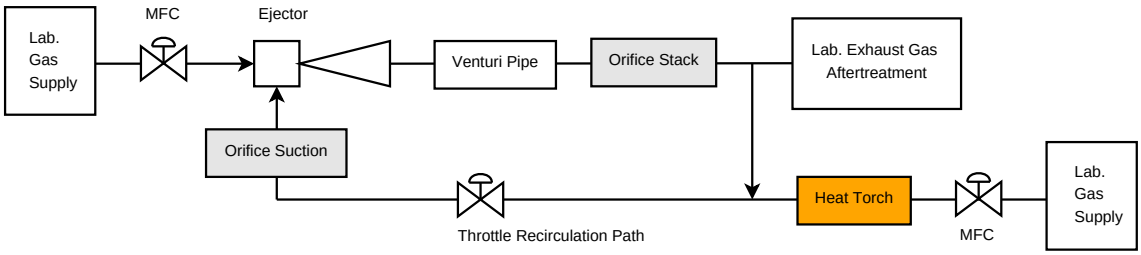

Figure 6.14: Test setup for parameter: System temperature

Figure 6.15 shows the negative impact of increasing the recirculated gas temperature. The air through the nozzle is being heated up by the hot recirculating gas of the ejector system. This rise in temperature leads to an increase of the viscosity (see Figure 6.19) resulting in a pressure loss over the nozzle. An other explanation of this effect is the thermal material extension of the Laval nozzle resulting in a smaller inner geometry and also a decreased cross sectional area of the nozzle throat. In a regular case, the nozzle would expand radially resulting in overall bigger dimensions. But this must not be the case as not all of the components are being heated up to the same amount because of fresh air flowing through the entrance of the nozzle. Both effects lead to a higher primary inlet pressure that is needed to accomplish a constant mass flow through the mass flow controller as well as the nozzle itself.

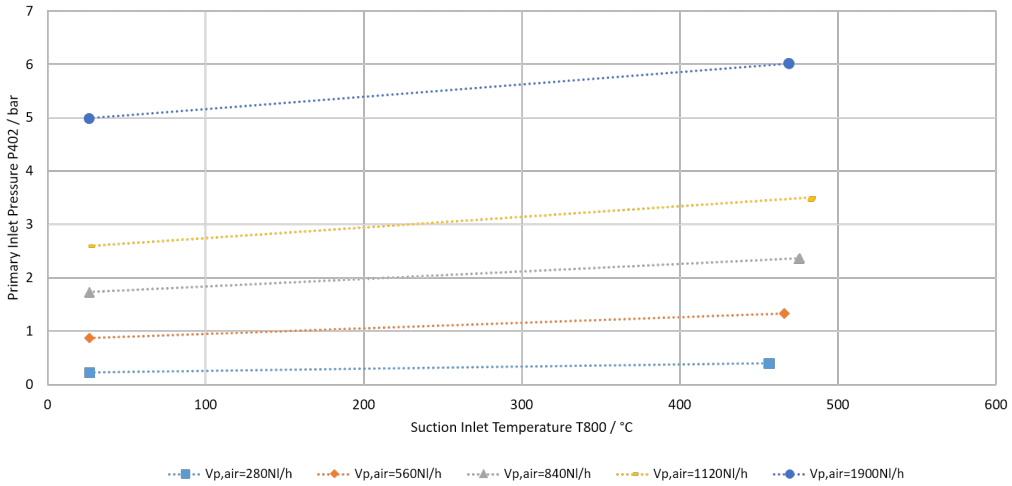

Figure 6.15: Primary Inlet Pressure vs. Suction Inlet Temperature
Ejector test system design A
26.04.2017

Figure 6.16 illustrates the temperature dependency of AGR_{O2}.

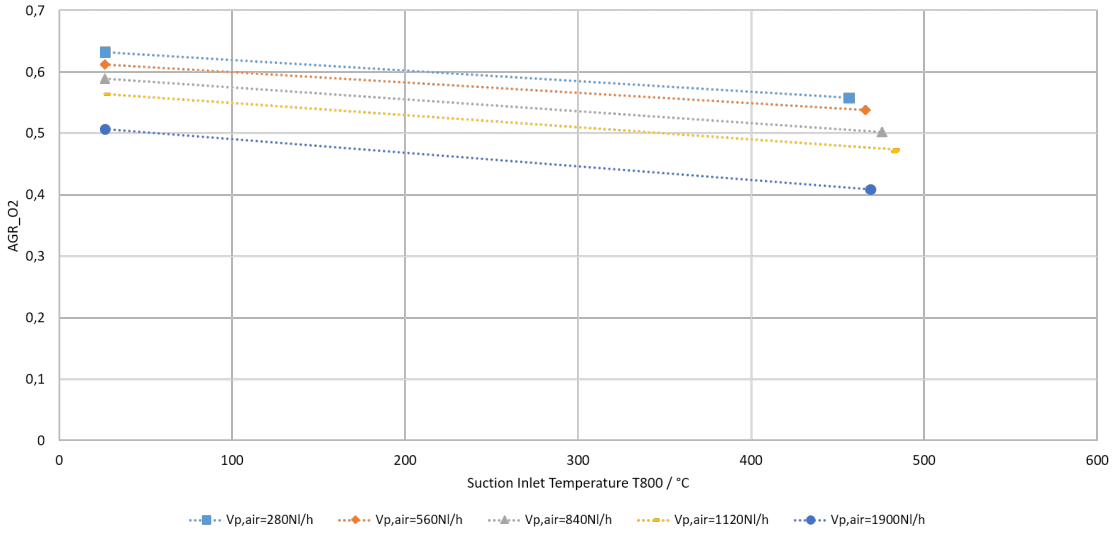

Figure 6.16: Anode-off Gas Recirculation Ratio (including O2) vs. Suction Inlet Temperature
Ejector test system design A
26.04.2017

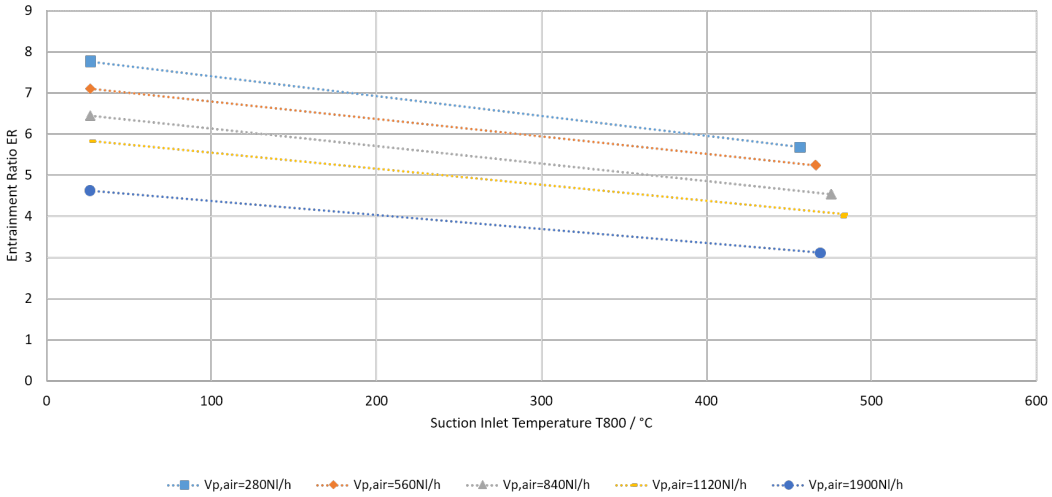

Figure 6.17: Entrainment Ratio vs. Suction Inlet Temperature
Ejector test system design A
26.04.2017

In Figure 6.18 the negative effect of the temperature increase of the recirculated gas is depicted. The discharge suction pressure $dP_{ejector}$ for various primary inlet flows $\dot{V}_{p,air}$ is increasing with temperature.

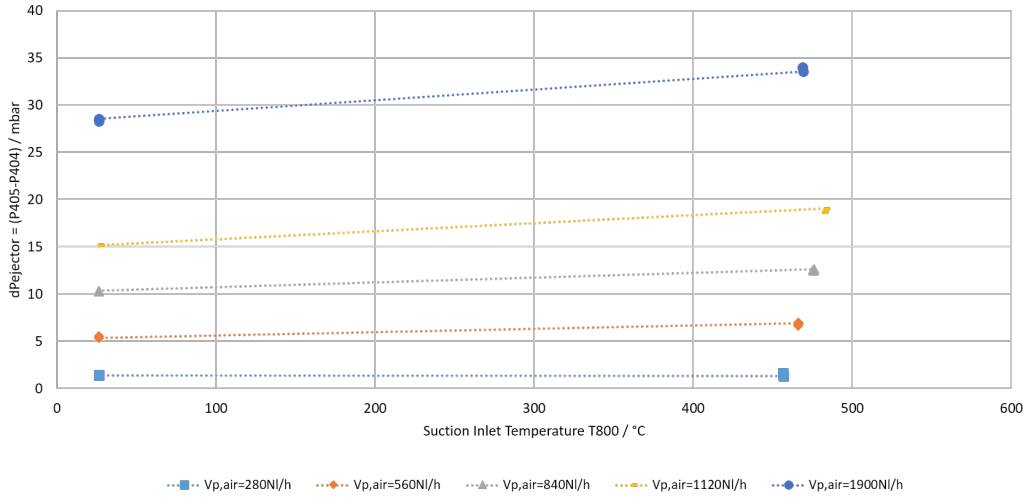

Figure 6.18: Discharge-Suction Pressure vs. Suction Inlet Temperature
Ejector test system design A
26.04.2017

Table 6.4: Parameter: System Temperature (**Ejector test system design A**)

$V_{p,air}$	$T800$	ER	AGR_{O2}	$dP_{ejector}$	$P402$	$AP400$
Nl/h	°C	-	-	mbar	bar	bar
280	26.5	7.78	0.63	1.4	0.231	0.964
	456.2	5.69	0.56	1.6	0.398	0.964
560	26.5	7.1	0.61	5.6	0.873	0.964
	465.9	5.25	0.54	6.9	1.330	0.964
840	26.4	6.45	0.59	10.3	1.730	0.964
	475.3	4.54	0.50	12.5	2.360	0.964
1120	26.4	5.83	0.56	15.2	2.600	0.964
	481.6	4.00	0.47	18.7	3.460	0.964
1900	26.2	4.64	0.51	28.4	4.990	0.964
	468.6	3.12	0.41	34.0	6.020	0.964

A defintion of viscosity as a fluid property is the following:

> *„Viscosity is a measure of a fluid's resistance to flow."* [41]

The influence of temperature to the absolute viscosity of air and methane is plotted in Figure 6.19. The increase of gas temperature inside of the system leads to a higher friction leading to a growing pressure drop as seen in Figure 6.18.

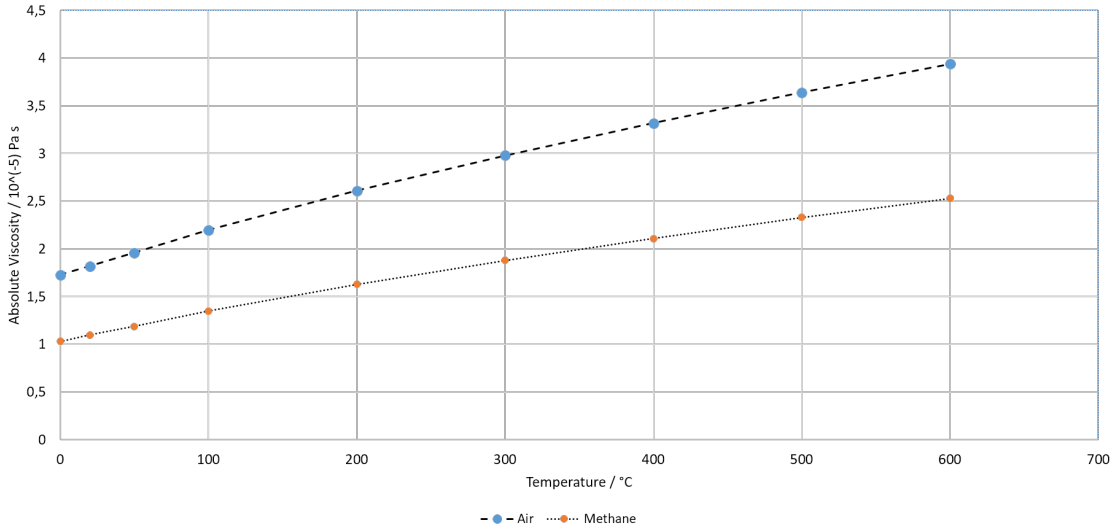

Figure 6.19: Absolute Viscosity of Air and Methane plotted against temperature [42]

6.2.7 Parameter: Gas type (air vs. methane)

Figure 6.20 shows the comparison of operating the ejector with either air or methane as a primary motive fluid. In order to have both options for the boundary conditions in the further CFD simulations, the measurements were performed for having the same mass flow.

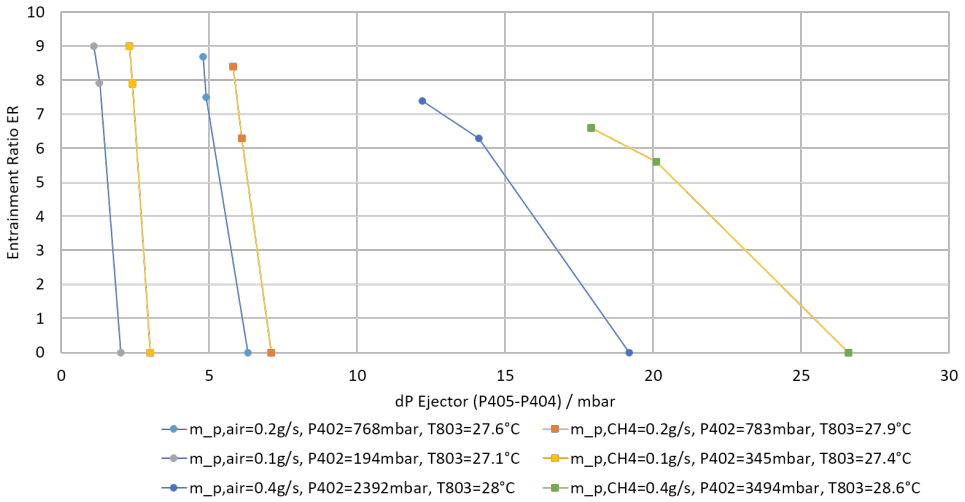

Figure 6.20: Comparison of the ejector performance for air and methane
Ejector test system design A

Figure 6.22 shows measurement results for the use of air and methane for several primary volume flows and for the open suction inlet and blocked suction inlet case. The difference in the primary inlet pressure for air and methane is coming from the difference in pressure of the used gas. The area between those two cases shows the possible operating area of the ejector.

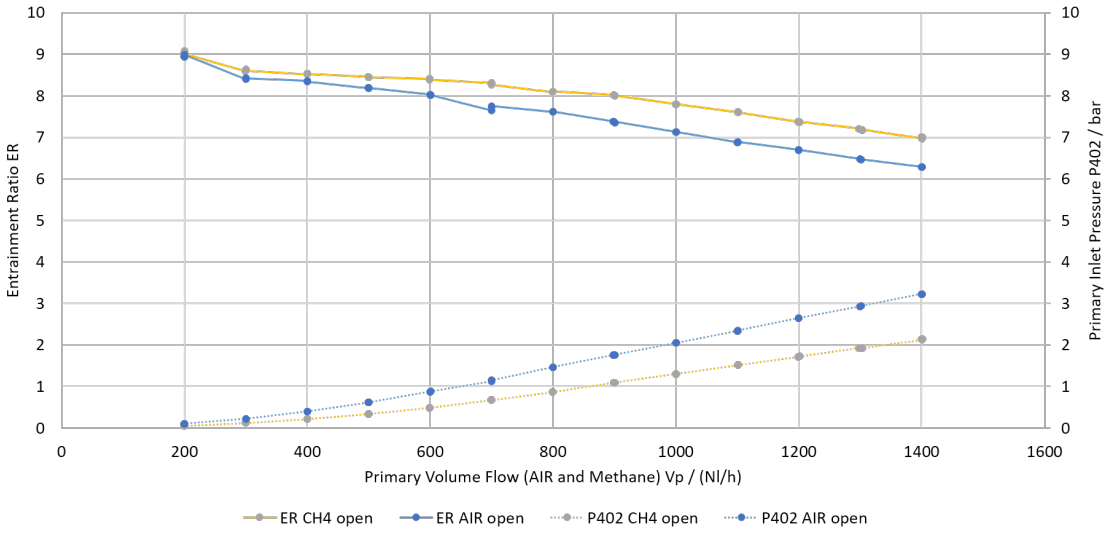

Figure 6.21: Comparison air vs. methane
Ejector test system design A
No orifices
20.06.2017

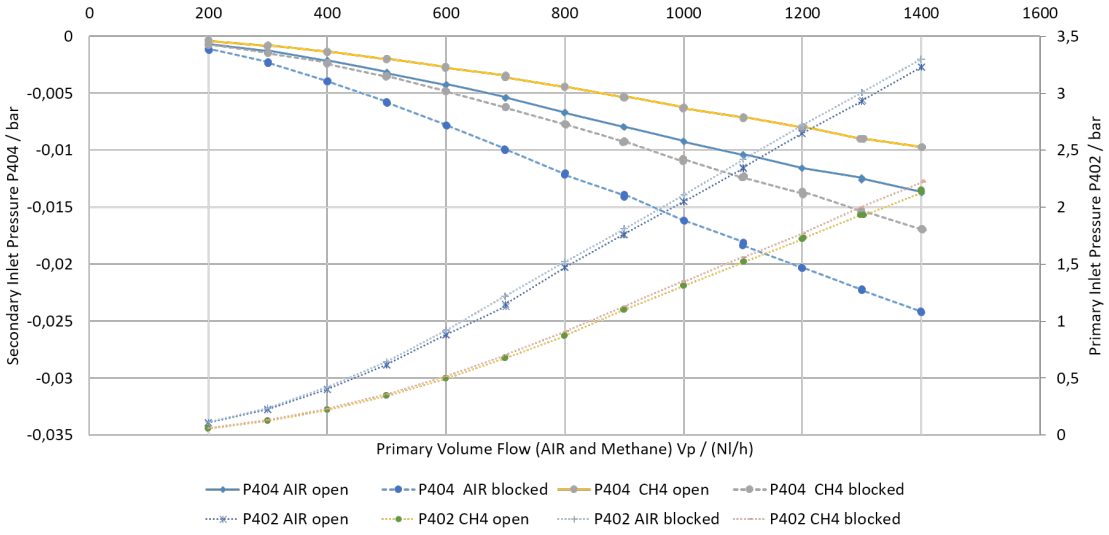

Figure 6.22: Comparison air vs. methane
Ejector test system design A
No orifices
20.06.2017

6.2.8 Parameter: Primary gas temperature

A further investigation is the influence of the primary gas inlet temperature. Heating cords on the primary inlet and also on the recirculation path are used for heating up the system. In order to prevent the insulation material from emitting smoke, the process of warming up was carried out at a rate of 10 °C / 60 s. In

the beginning of the test, only the primary inlet gas was heated up, but not the recirculation path. Reaching temperatures of the primary gas of about 230 °C the insulation started to smoke heavily making it impossible to reach higher temperatures in this test.

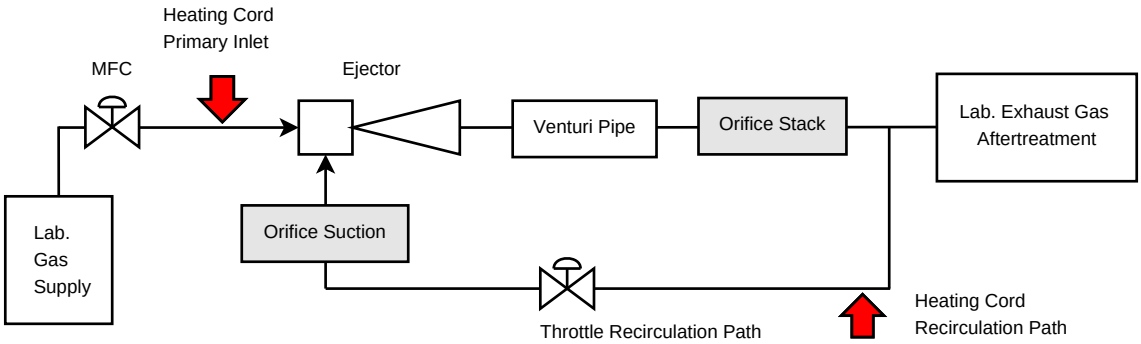

Figure 6.23: Test rig setup for heating up the primary inlet gas (air)
06.20.2017
Ejector test system design A

The graph in Figure 6.24 shows three regions. In the first region only the cord is activated which heats up the primary inlet gas. The entrainment ratio is increasing until the second region is reached. The heating cord in the recirculation path is activated and the recirculated gas is heated up. In this region the entrainment ratio stops increasing. Finally in the third region, the primary inlet heating cord is deactivated. Now the entrainment ratio is decreasing again showing the negative input of a high system temperature because of friction inside the recirculation path.

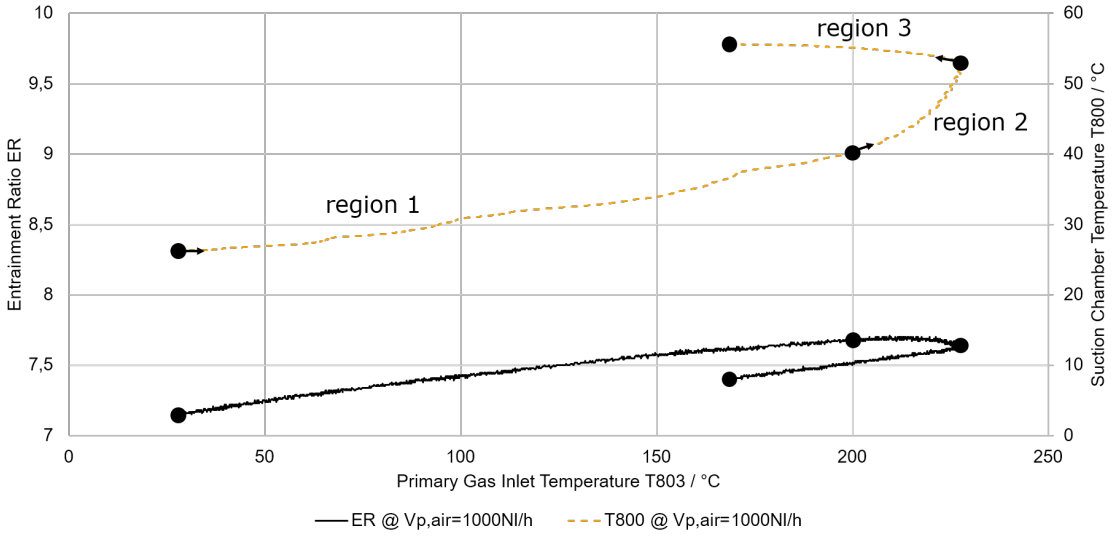

Figure 6.24: Heating up primary inlet gas (air)
AP400 = 0.976 mbar
Ejector test system design A
20.06.2017 14:25

6.3 Ejector test system design B

In this section all the measurement results with respect to the **Ejector test system design B** are described. The basic design informations are stated in Figure 6.1:

Nozzle 1: Nozzle throat diameter $d_T = 0.58\,\text{mm}$
Nozzle 1: Nozzle exit diameter $d_{NE} = 0.91\,\text{mm}$
Ejector 2: Mixing chamber diameter $d_c = 6\,\text{mm}$
Ejector 2: Mixing chamber length $l_c = 67.09\,\text{mm}$
Position: $x_0 + \Delta x$

Figure 6.25: Main design parameters of **Ejector test system design B** [12]

6.3.1 Parameter: Nine nozzle holder positions

Figure 6.26 shows how the entrainment ratio is changing with the different positions of the nozzle holder for the **Ejector test system design B**. One complete turn of the mixing chamber results in a change in distance of 1.5 mm. One turn is displayed with the symbol U. Because of a missing mechanical part (lock–nut M30) that would be needed to fix the mixing chamber solid in one position to make several other changes, the position $x_0 + 2U$ was used for all further investigations on the **Ejector test system design B**.

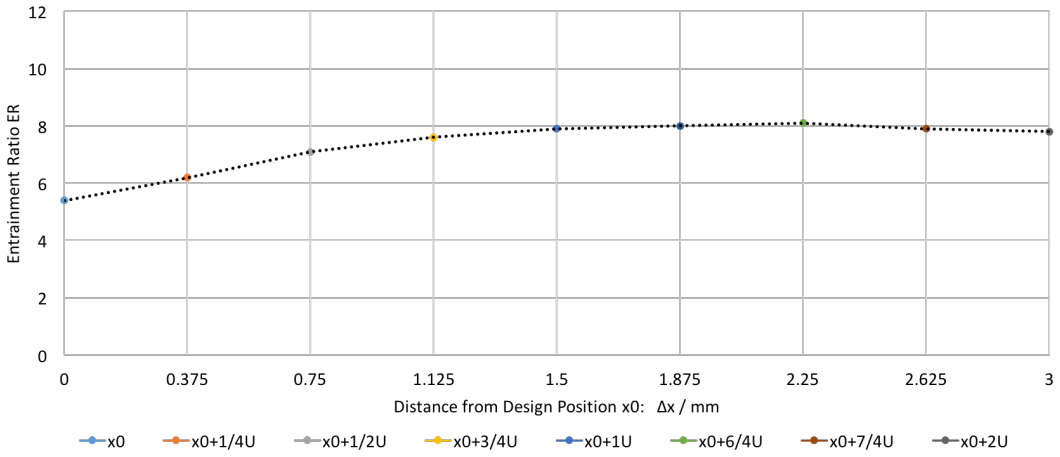

Figure 6.26: optimal nozzle holder position
$\dot{V}_{p,air} = 560\,\text{Nl/h}$
Ejector test system design B

Table 6.5: Position Variation (**Ejector test system design B**)

Position Name	Δx	ER	$\dot{V}_{p,air}$	$dP_{ejector}$	$\frac{ER_{max}-ER}{ER_{max}}$
-	mm	1	Nl/h	mbar	%
x_0	0	5.4	560	3.7	67
$x_0 + \frac{1}{4}U$	0.375	6.2	560	5.0	77
$x_0 + \frac{1}{2}U$	0.750	7.1	560	5.4	88
$x_0 + \frac{3}{4}U$	1.125	7.6	560	6.6	94
$x_0 + 1U$	1.500	7.9	560	7.8	98
$x_0 + \frac{5}{4}U$	1.875	8	560	8.0	99
$x_0 + \frac{6}{4}U$	2.250	8.1	560	8.1	100
$x_0 + \frac{7}{4}U$	2.625	7.9	560	7.9	98
$x_0 + 2U$	3.00	7.8	560	7.8	96

Figure 6.27 shows the behaviour of the **Ejector test system design B** for different primary volume flows in the design position. The throttle in the recirulation path was slowly closed in order to reach a blocked suction inlet.

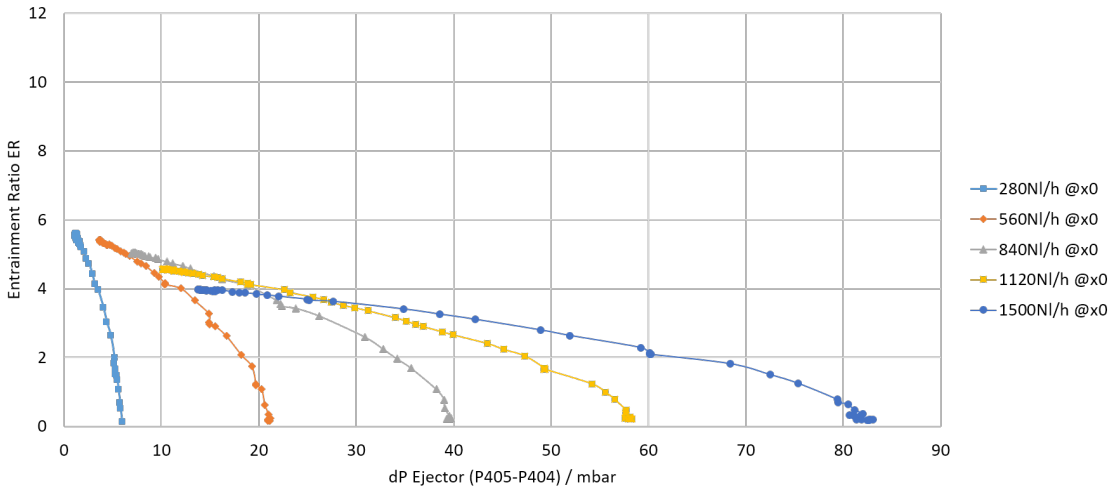

Figure 6.27: Nozzle holder position x_0
Ejector test system design B

The experiment was repeated for different positions of the nozzle holder and the results are shown in Figure 6.28. The entrainment ratio is increased but

the maximum reached discharge suction pressure stays relatively constant in comparison.

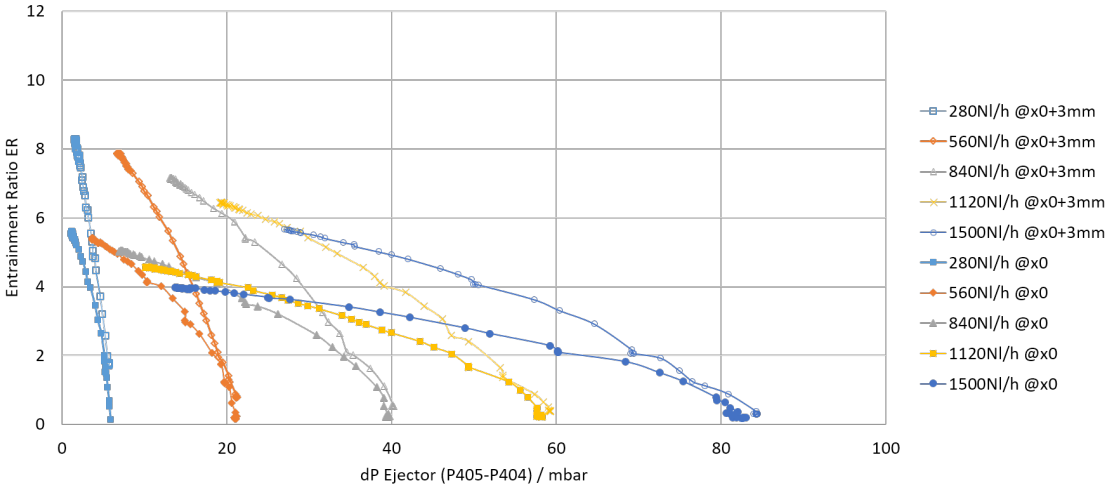

Figure 6.28: Nozzle holder position x_0 and $x_0 + 2U$
Ejector test system design B

6.4 Comparison of the Ejector test system designs

As shown in Figure 3.1 the ejector test system designs do have a major difference compared to the ejector development designs. The nozzle of both systems is the same. The main parameters are shown in Table 6.6. For comparing the different designs, the measurements were performed at the optimum operating positions for each design.

Table 6.6: Main parameters of the Ejector test system designs

		Ejector test system design	
		A	**B**
Nozzle throat diameter	d_T	0.80 mm	
Nozzle exit diameter	d_{NE}	0.87 mm	
Ejector mixing chamber diameter	d_c	10.50 mm	6.00 mm
Ejector mixing chamber length	l_c	70.40 mm	67.09 mm
Position	$x_0 + \Delta x$	$x_0 + 4.5$ mm	$x_0 + 3.0$ mm

Lowering the mixing chamber diameter from **design A** to **design B** results in a lower entrainment ratio for the same nozzle and primary volume flow. The relation between the entrainment ratio and $dP_{ejector}$ is more flat in **design B**. This system has therefore a higher operating range and stability with respect to the pressure drop along the anode and recirculation path.

The cumulated comparison results are shown in Figure 6.29.

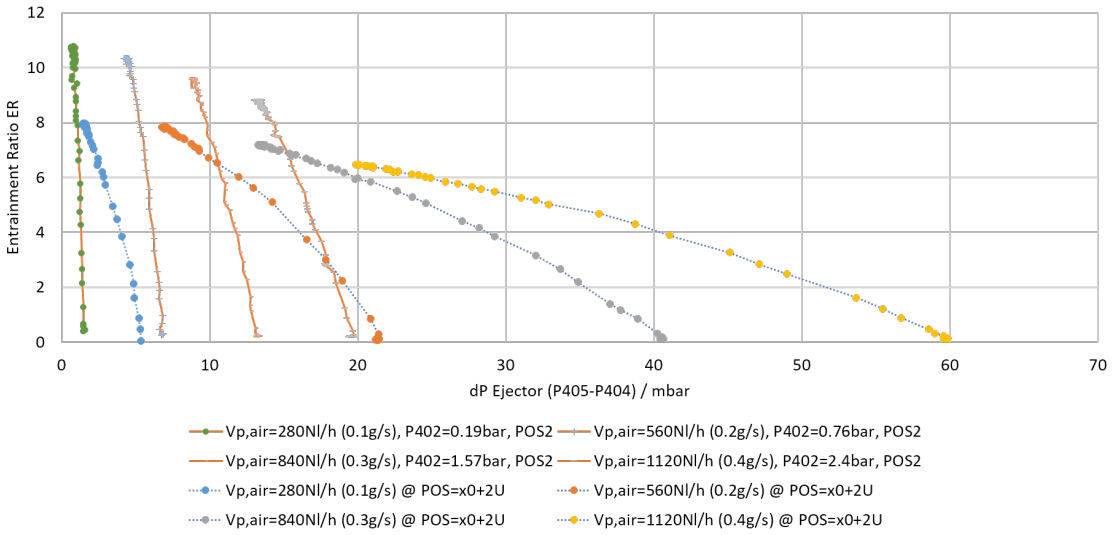

Figure 6.29: Comparison of the test system designs for different $\dot{V}_{p,air}$
Ejector test system design A
Ejector test system design B

From Figure 6.30 to Figure 6.33 the results are shown in detail for one primary volume flow and both of the designs.

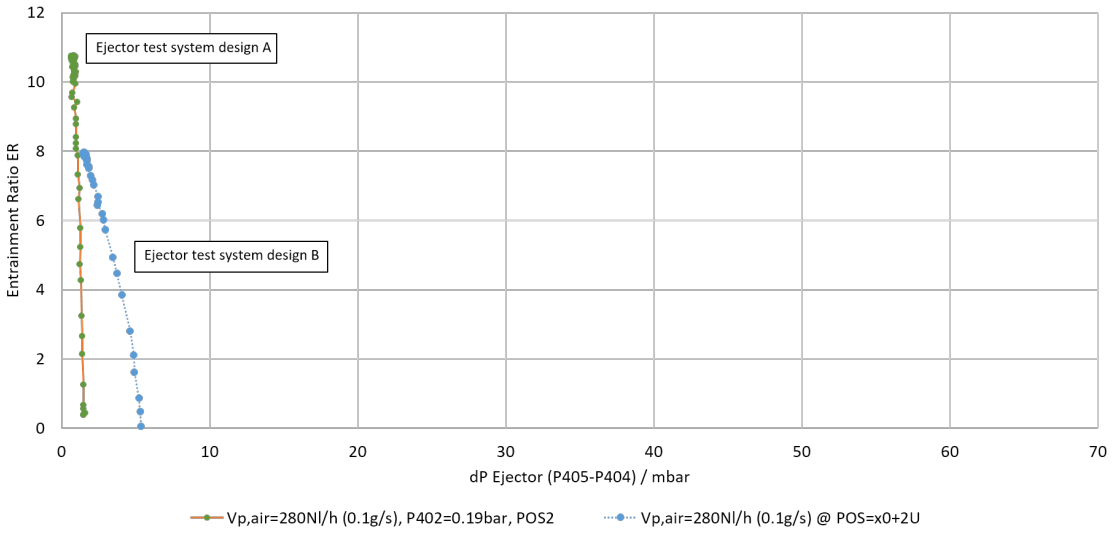

Figure 6.30: Comparison of the test system designs for $\dot{V}_{p,air} = 280\,\mathrm{Nl/h}$
Ejector test system design A
Ejector test system design B

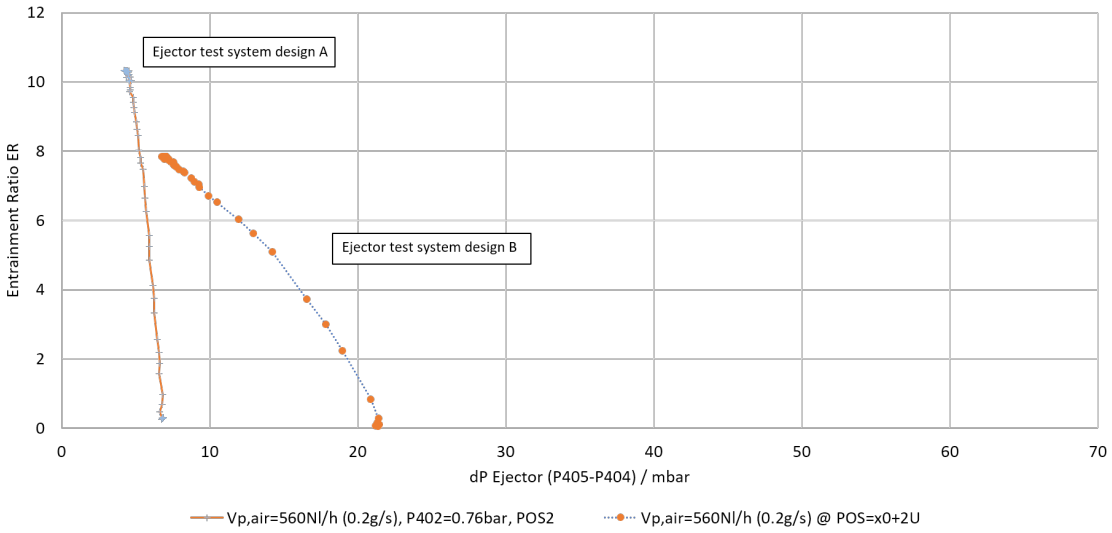

Figure 6.31: Comparison of the test system designs for $\dot{V}_{p,air} = 560\,\mathrm{Nl/h}$
Ejector test system design A
Ejector test system design B

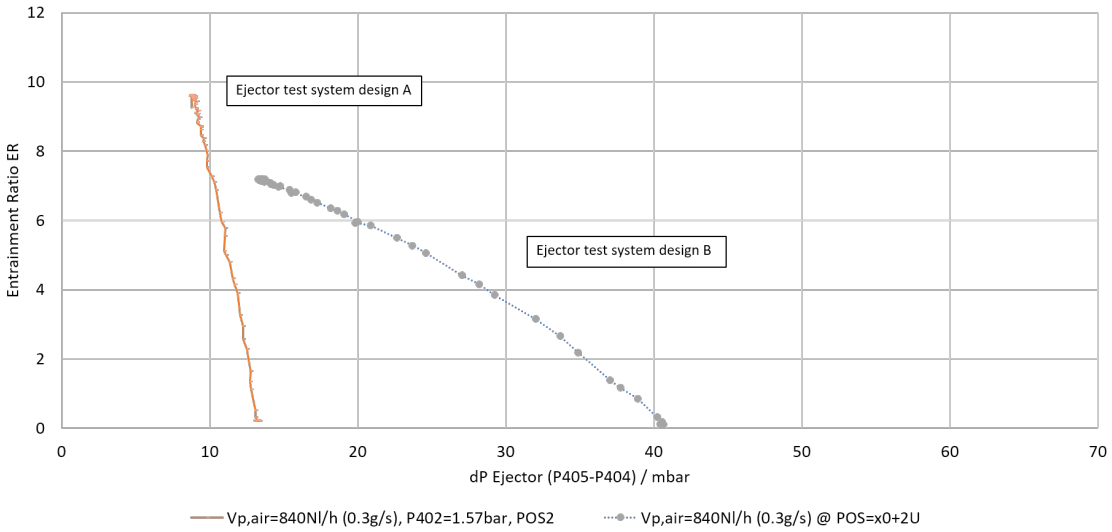

Figure 6.32: Comparison of the test system designs for $\dot{V}_{p,air} = 840\,\mathrm{Nl/h}$
Ejector test system design A
Ejector test system design B

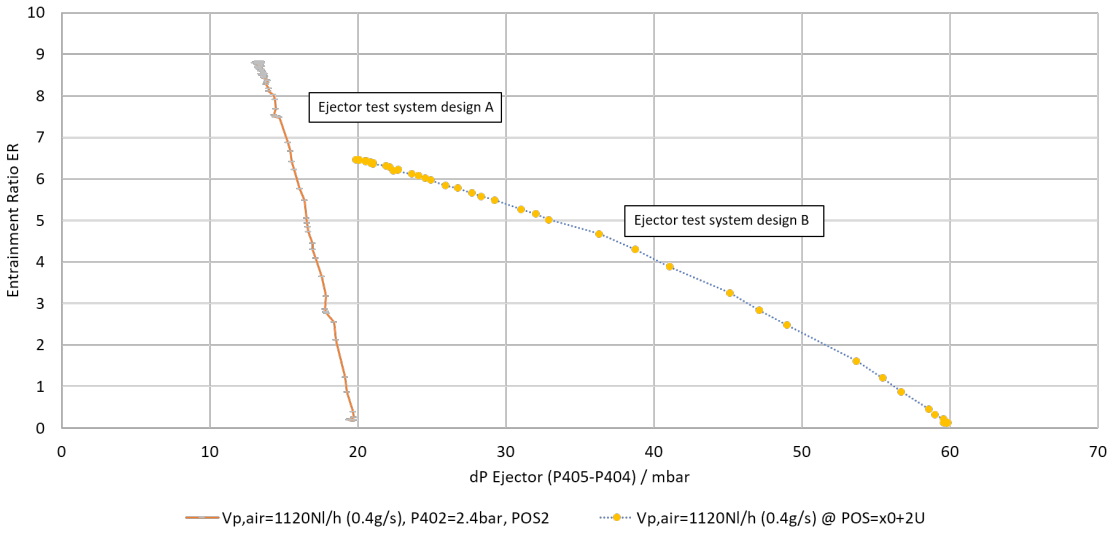

Figure 6.33: Comparison of the test system designs for $\dot{V}_{p,air} = 1120\,\mathrm{Nl/h}$
Ejector test system design A
Ejector test system design B

6.5 Ejector test system CFD simulation

In the following section the ejector test system simulation results are presented regarding the development process depicted in Figure 3.1. In the beginning of M. Tkaucic's simulations the layout in Figure 6.35 was used, which is compared to the simulations done by M. Rossi already a big improvement in terms of comparability to the measurements.

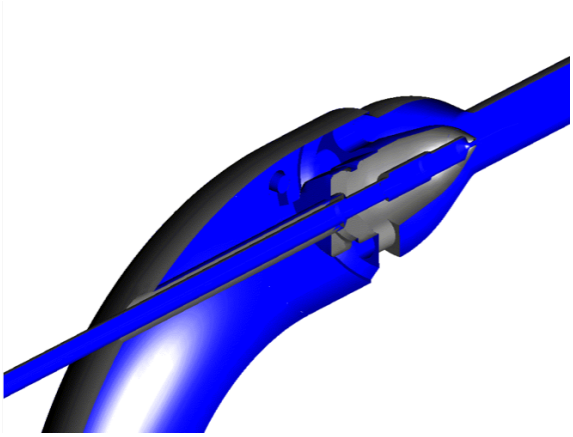

Figure 6.34: CFD simulation layout [43]
Ejector test system design A

Moreover, the meshing was adapted to create more detailed and therefore more reliable results. The Figures 6.35 and 6.36 illustrate the refinement of the mesh according to areas of special interest.

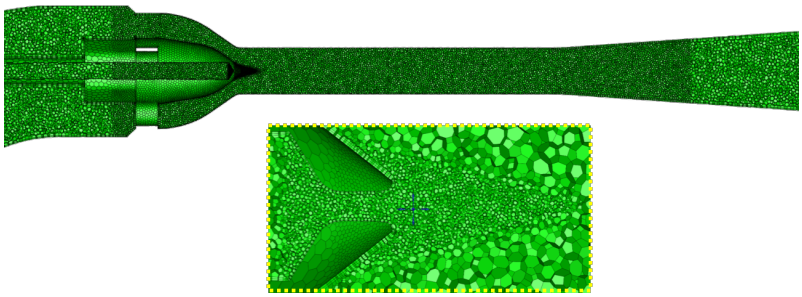

Figure 6.35: CFD simulation layout meshing topology (Zoom: Nozzle exit) [43]
Ejector test system design A

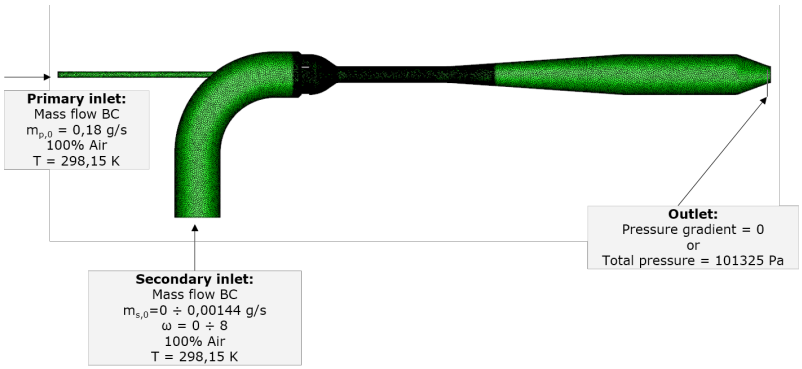

Figure 6.36: CFD simulation layout, boundary conditions and meshing [43]
Ejector test system design A

Proceedingly the simulation layout of M. Tkaucic including his boundary conditions was improved. He used the CAD information from C. Sallai and created a layout represeting the real **Ejector test system design A**. More information can be found in Figure 6.37.

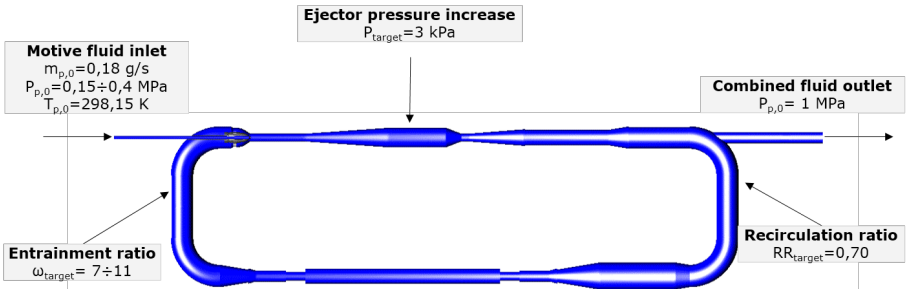

Figure 6.37: CFD simulation layout and ejector boundary conditions [43]
Ejector test system design A

The different sections regarding the simulation layout of M. Tkaucic with respect to the improved layout of Figure 6.37 are displayed in Figure 6.38.

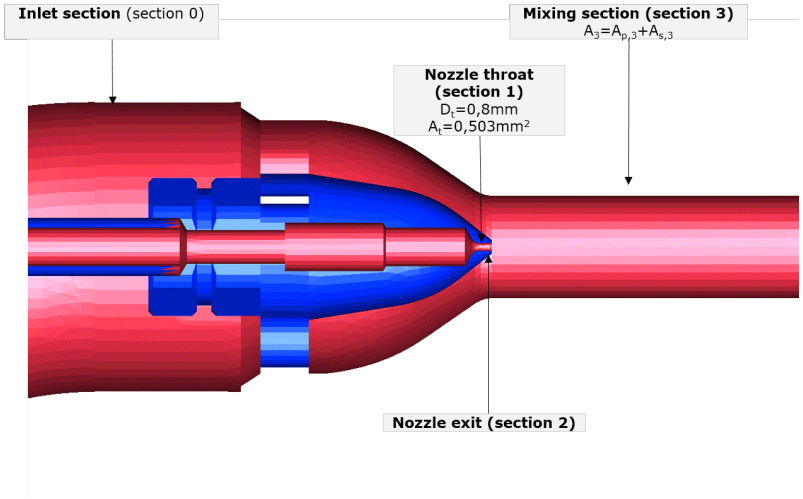

Figure 6.38: Simulation layout with Laval nozzle including sections [43]
Ejector test system design A

As already mentioned in Section 4.7 the diffusor of the nozzle 1 was shortened in order to overcome to problem of having a shockwave inside of the nozzle. The simulations done by M. Tkaucic revealed what was a logical consequence of this action. The diverging part of the nozzle is too short in order to reach Mach-numbers that are reasonably higher than $M = 1$ as display in Figure 6.39.

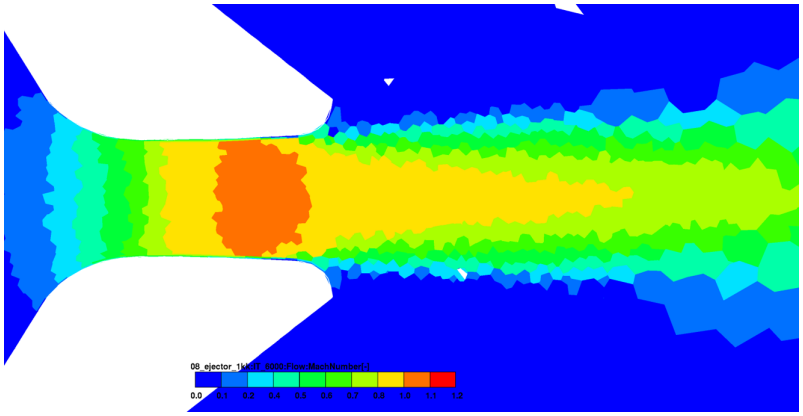

Figure 6.39: Mach number in the nozzle throat, maximum Ma≈1.03 [43]
Ejector test system design A

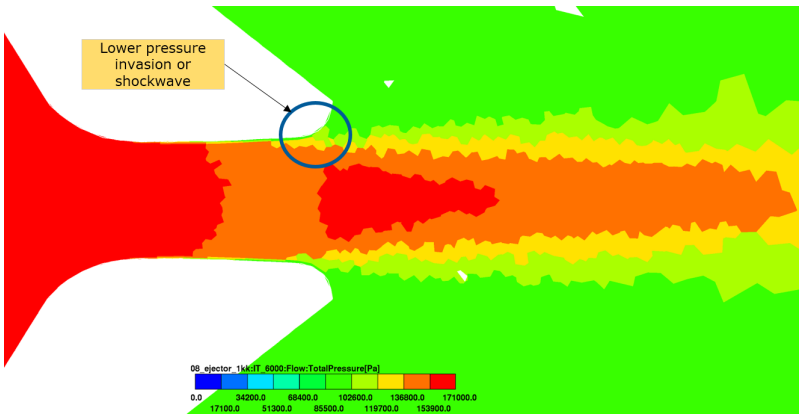

Figure 6.40: Pressure Graph [43]
Ejector test system design A

The comparison of the measurements done in the laboratory and the CFD simulations performed by M. Tkaucic are shown in Figure 6.41. They show a good match which was the base for all the other design investigations and sensitivity analysis done in the CFD department based on the experimental validation. The boundary conditions are shown in Figure 6.36.

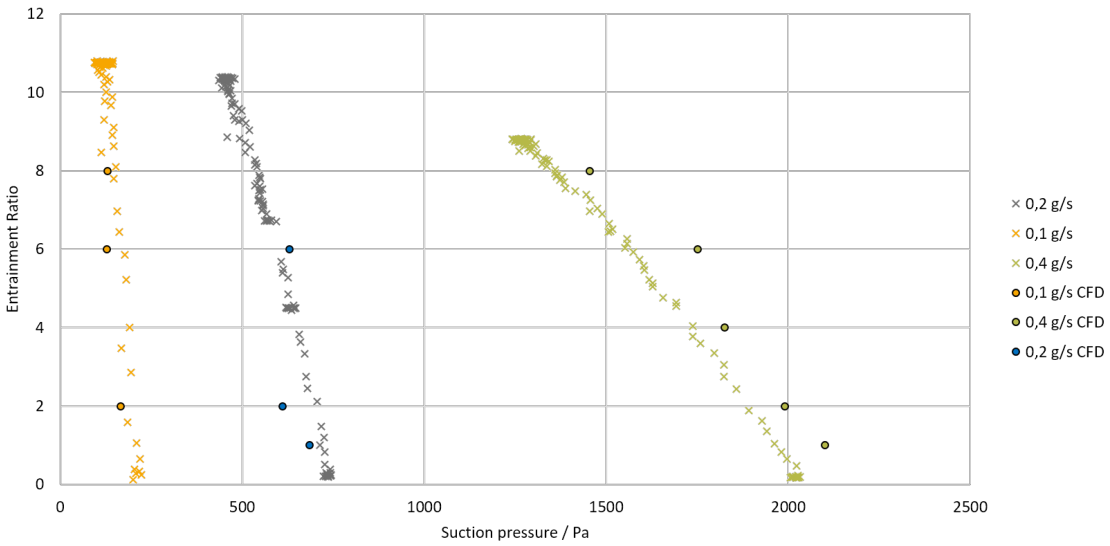

Figure 6.41: Comparison of measurement and CFD results [43]
Ejector test system design A

The high quality and level of detail in the graphs of Figure 6.42 and Figure 6.43 makes evaluates possible. As already described in Section 6.4 the effect of modifying the mixing chamber diameter to the ejector behaviour is enormous. The size of expansion stream coming off the nozzle is too small for a stable and solid functioning of the ejector. Figure 6.43 indicates a smaller mixing chamber as it was realized in **Ejector test system design B**.

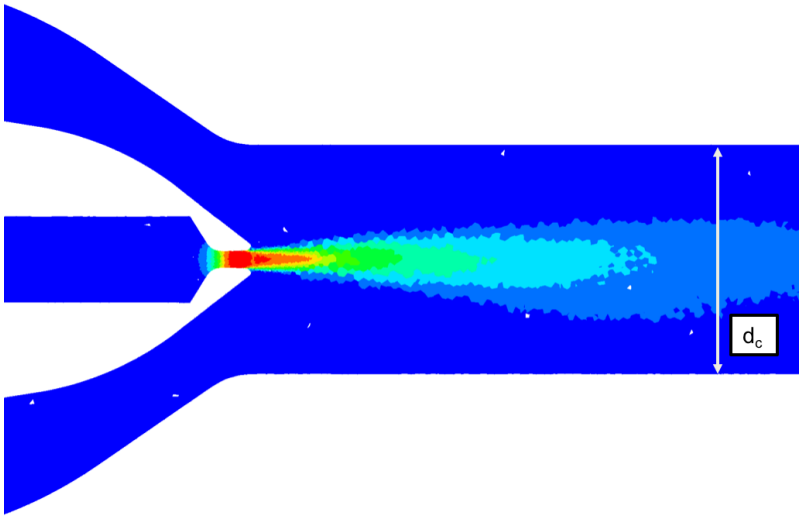

Figure 6.42: Velocity graph and mixing chamber [43]
(**Ejector test system design A**)
$d_c = 10.50\,\text{mm}$

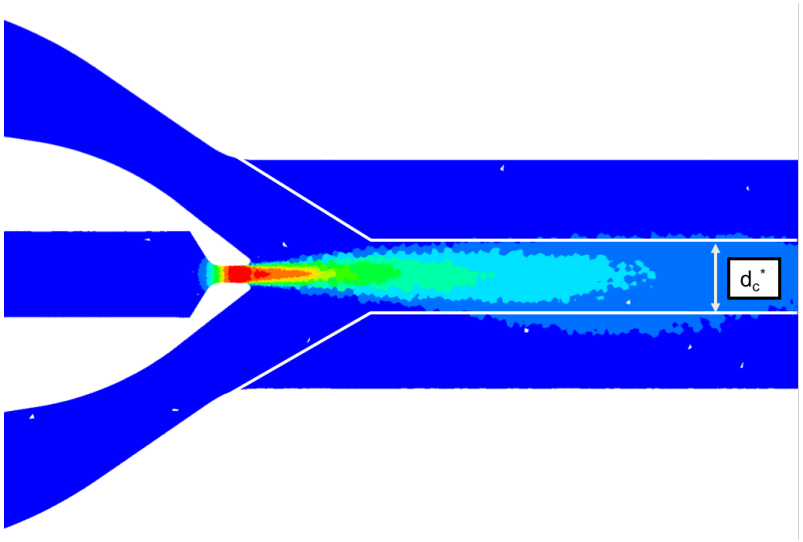

Figure 6.43: Velocity graph and mixing chamber [43]
(**Ejector test system design A**)
(indicating a smaller diameter d_c^*)

7 Conclusion

In this chapter a summary of the experiments is presented. Encounter problems are described and ideas for further investigations are explained.

7.1 Parameter study and results

Figure 3.1 in Section 3 shows the development process of the ejector for SOFC applications. Two different designs have been simulated using altered constructional parameters for the nozzle and the ejector part each. At first, one of these designs was constructed and tested. After gaining a lot of knowledge through the measurements, the decision was made to retain the Nozzle 1 and to change only the ejector part to the second design. Otherwise it is hardly impossible to make assertions of the influence of the mixing chamber diameter and length on the ejector performance.

The following performance-affecting parameters have been investigated through the experiments in the laboratory and are documented in the thesis:

- Nozzle position
- Pressure drop in the anode recirculation path
- Pressure drop in the anode path
- Exhaust choking
- Effect of recirculation gas temperature
- Gas types (Air & Methane)
- Mixing chamber diameter
- Primary inlet gas temperature

Both ejector designs do not meet the requirements for efficient AGR in the analyzed SOFC system. This is because they are not capable of providing the needed performance which is to guarantee an entrainment ratio of $ER = 11$ for different pressure drops in the system. The parameter study (experimental validation) should help understanding the principles and serve as a reference for further design improvements based on the CFD simulations.

For all of the different parameter variations stable flow conditions were achieved. There have been no indications in the measurement data or in the sound emissions during the test on a pulsating flow or other types of instability.

7.2 Test rig handling improvements

The test rig setup can be improved by changing the position of the Venturi pipe from the anode path to the anode recirculation path. Thereby, time can be saved when the test setup is turned for detecting the optimum distance between nozzle and mixing chamber. For future tests an automation of the primary inlet volume flow control is highly recommended. Switching between two different values requires at least five seconds until the actual value has settled on the setpoint value of the mass flow controller.

7.3 Outlook

A further increase in performance of the ejector system through design improvements is very probable and is already under investigation. The effect of the nozzle and mixing chamber design are studied further. In addition, a multiple stage ejector topology could be used to provide enough power an flexibility. Further research topics will deal with the CFD simulation of the real gas composition and the influence of the high temperatures on the ejector. A combination of an ejector and a blower for recirculation of the anode-off gas would also be possible.

List of Figures

List of Tables

Bibliography

[1] James Larminie, Andrew Dicks. *Fuel Cell Systems Explained*. 2003 (cit. on pp. 1–5, 9, 19).

[2] Simone Lion. "Celle a combustibile. Applicazioni e impatto ambientale." Bachelor's Thesis. University of Padova, 2010 (cit. on p. 1).

[3] Johannes Töpler and Jochen Lehmann. *Wasserstoff und Brennstoffzelle - Technologien und Marktperspektiven*. With a forew. by Ernst Ulrich von Weizsäcker. Springer-Verlag Berlin Heidelberg 2014, 2014. ISBN: 978-3-642-37414-2. DOI: 10.1007/978-3-642-37415-9 (cit. on p. 5).

[4] U.S. Department of Energy. *Comparison of Fuel Cell Technologies*. Mar. 28, 2017. URL: https://www1.eere.energy.gov/hydrogenandfuelcells/fuelcells/pdfs/fc_comparison_chart.pdf (visited on 03/28/2017) (cit. on p. 6).

[5] Fuel Cell & Hydrogen Energy Association. *Fuel Cell & Hydrogen Energy Association*. URL: http://www.fchea.org/fuelcells/ (visited on 03/28/2017) (cit. on pp. 6–8).

[6] Wikipedia Commons. *Diagram of a solid oxide fuel cell*. Ed. by Sakurambo. Oct. 16, 2017. URL: https://commons.wikimedia.org/wiki/File:Solid_oxide_fuel_cell.svg (visited on 03/28/2017) (cit. on p. 8).

[7] Adam Hawkes, Iain Staffell, Dan Brett, Nigel Brandon. "Fuel cells for micro-combined heat and power generation." In: *Royal Society of Chemistry* (Apr. 19, 2009). URL: http://pubs.rsc.org/en/Content/ArticleHtml/2009/EE/b902222h (cit. on pp. 10, 11).

[8] AVL List GmbH, Austria, Martin HAUTH. "Internal Documents." 2017 (cit. on pp. 11, 12).

[9] J. Rechberger, M. Hauth and M. Reissig. *SOFC System Development and Testing, Fuel Cell Seminar*. Tech. rep. Uncasville CT U.S., 2012 (cit. on p. 12).

[10] Simone Lion. "System Scale Up of a Stationary 10 kW SOFC CHP Unit." Masters Thesis. Universita degli Studi di Trieste, 2013 (cit. on p. 13).

[11] J. Rechberger, M. Reissig, M. Hauth. "AVL SOFC Systems on the Way of Industrialization." In: *The Electrochemical Society* (2013) (cit. on p. 13).

[12] Mirko Rossi. "Development of ejector based anode gas recirculation for a SOFC system." MA thesis. Università degli Studi dell'Aquila, 2017 (cit. on pp. 15, 16, 26–29, 44, 59).

[13] CHAQING LIAO. "GAS EJECTOR MODELING FOR DESIGN AND ANALYSIS." PhD thesis. Office of Graduate Studies of Texas A&M University, 2008 (cit. on pp. 15, 19, 20).

[14] Matej Tkaucic. "Master Thesis (in progress)." Master Thesis. 2017 (cit. on p. 16).

[15] R. Castelnuovo. *Sectional view of a steam ejector*. 2007. URL: https://commons.wikimedia.org/wiki/File:Ejector.PNG (cit. on p. 17).

[16] Ronan K. McGovern. "One-dimensional Model of an Optimal Ejector and Parametric Study of Ejector Efficiency." In: (2012) (cit. on p. 18).

[17] The Engineering ToolBox. *STP - Standard Temperature and Pressure*. Feb. 11, 2017. URL: http://www.engineeringtoolbox.com/stp-standard-ntp-normal-air-d_772.html (visited on 01/11/2017) (cit. on pp. 19, 43).

[18] Yinhai Zhu, Wenjian Cai, Changyun Wen, Yanzhong Li. "Fuel ejector design and simulation model for anodic recirculation SOFC system." In: *J. Power Sources 173 (2007) 437-449* (2007). URL: http://www.sciencedirect.com/science/article/pii/S0378775307015935?via%3Dihub (cit. on pp. 19, 20).

[19] Maximilian Engelbracht, Roland Peters, Ludger Blum, Detlef Stolten. "Comparison of a fuel-driven and steam-driven ejector in solid oxide fuel cell systems with anode off-gas recirculation: Part-load behavior." In: *Journal of Power Sources 277 (2015) 251e260* (2014) (cit. on p. 20).

[20] B. D. Power, New York. *High Vacuum Pumping Equipment*. Reinhold Publishing Corporation, 1966 (cit. on p. 21).

[21] Chicago Faucets. *Full Flow Aspirator Pump Serrated Outlet*. Oct. 3, 2017. URL: http://www.chicagofaucets.com/images/catalog/highres/E17JKRCF.jpg (cit. on p. 21).

[22] Lockemann, G. *The centenary of the Bunsen burner*. Journal of Chemical Education, vol. 33, issue 1, p. 20, 1956. DOI: 10.1021/ed033p20 (cit. on p. 21).

[23] Wikimedia Commons. *File:Bunsen burner.jpg*. Ed. by User: Deglr6328. Sept. 11, 2017. URL: https://commons.wikimedia.org/wiki/File:Bunsen_burner.jpg (cit. on p. 21).

[24] Parramon and Ferron. *The Big Book of Airbrush*. 1990 (cit. on p. 22).

[25] Pixabay.com. *Airbrush Kunst Pinsel Design Farbe*. Oct. 3, 2017. URL: https://pixabay.com/de/airbrush-kunst-pinsel-design-farbe-156988/ (cit. on p. 22).

[26] Smil Vaclav. *Creating the twentieth century: technical innovations of 1867–1914 and their lasting impact*. Oxford University Press US, 2005. ISBN: 978-0-19-516874-7 (cit. on p. 22).

[27] Georg Langer Verzinkerei GmbH & Co KG. *Sandstrahlen*. Ed. by Georg Langer. Sept. 12, 2017. URL: http://www.verzinkerei-langer.de/Sandstrahlen.html (cit. on p. 22).

[28] J. Fernandez Puga, S. Fleck, M. Mayer, F. Ober, T. Stengel, F. Ebert. "CFD-Simulation der Strömung in und nach einer Laval–Düse." In: *Chemie Ingenieur Technik* (2002) (cit. on p. 22).

[29] Lindermeir, Ralph-Uwe Dietrich, Christoph Immisch. *PROPANE DRIVEN HOT GAS EJECTOR FOR ANODE OFF GAS RECYCLING IN A SOFC-SYSTEM*. Ed. by Narottam P. Bansal and Mihails Kusnezoff. John Wiley & Sons, Inc., 2014 (cit. on p. 23).

[30] Young, Donald F. , Bruce R. Munson et al. *A Brief Introduction to Fluid Mechanics (5 ed.)* John Wiley & Sons, 2010. ISBN: 978-0-470-59679-1 (cit. on p. 23).

[31] National Aeronautics and Space Administration. *Nozzle Design Converging-Diverging (CD) Nozzle*. Ed. by Nancy Hall (Glenn Research Center). URL: https://www.grc.nasa.gov/www/k-12/airplane/nozzled.html (cit. on p. 23).

[32] Mario L. Ferrari, Davide Bernardi, Aristide F. Massardo. *Design and Testing of Ejectors for High Temperature Fuel Cell Hybrid Systems*. Tech. rep. Thermochemical Power Group (TPG), Università di Genova (Italy), 2006 (cit. on p. 32).

[33] National Instruments. *CompactRIO*. Ed. by NI. June 28, 2017. URL: http://www.ni.com/newsletter/50704/en/ (visited on 06/28/2017) (cit. on p. 37).

[34] Biezl. *MFC (Mass Flow Controller) Internal Block Diagram*. Ed. by Biezl. June 28, 2017. URL: https://en.wikipedia.org/wiki/Mass_flow_controller#/media/File:MFC_en.svg (cit. on p. 39).

[35] Wikipedia. *Venturi effect — Wikipedia, The Free Encyclopedia*. 2017. URL: https://en.wikipedia.org/w/index.php?title=Venturi_effect&oldid=795165368 (cit. on p. 39).

[36] Wikimedia Commons contributors. *File:Venturifixed.PNG*. Ed. by the free media repository. Wikimedia Commons. 2017. URL: https://commons.wikimedia.org/w/index.php?title=File:Venturifixed.PNG&oldid=153448533 (cit. on p. 39).

[37] Marika Natalie Gasteiger. *Venturi construction drawing AVL/AT* (cit. on p. 40).

[38] The Engineering ToolBox. *Density of air*. Jan. 11, 2017. URL: http://www.engineeringtoolbox.com/air-density-specific-weight-d_600.html (visited on 01/11/2017) (cit. on p. 43).

[39] The Engineering ToolBox. *Density of methane*. Jan. 11, 2017. URL: http://www.engineeringtoolbox.com/gas-density-d_158.html (visited on 01/11/2017) (cit. on p. 43).

[40] C. Sallai. *Construction drawings AVL/AT* (cit. on p. 45).

[41] Princeton.edu. *Viscosity Defintion (Gasdynamic)*. Oct. 2, 2017. URL: https://www.princeton.edu/~gasdyn/Research/T-C_Research_Folder/Viscosity_def.html (cit. on p. 55).

[42] Engineering ToolBox. *Gases Absolute Dynamic Viscosity*. URL: http://www.engineeringtoolbox.com/gases-absolute-dynamic-viscosity-d_1888.html (visited on 02/02/2017) (cit. on p. 55).

[43] Matej Tkaucic. "Project: DFE4909 3063 Gas ejector CFD analysis." Project. AVL/AT PTE-DAC, 2017 (cit. on pp. 64–68).